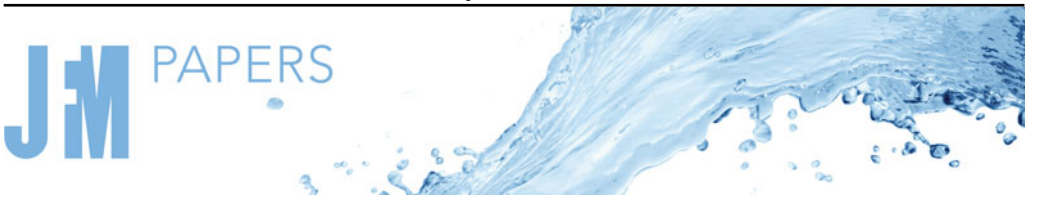
J. Fluid Mech. (2026), *vol.* 1042, A16, doi:10.1017/jfm.2026.11974



Spanwise twisting optimises flapping wing propulsive efficiency through force reallocation and the leading-edge vortex growth regulation

Ruishu Jin[1,2], **Qiuxiang Huang**[2,3,4], **Xueyu Ji**[2], **Gerald G. Pereira**[1] and **Fang-Bao Tian**[2]

[1]CSIRO Technology, Private Bag 10, Clayton South, VIC 3169, Australia

[2]School of Engineering and Technology, University of New South Wales, Canberra, ACT 2600, Australia

[3]School of Mechanical, Medical and Process Engineering, Queensland University of Technology, Brisbane, QLD 4000, Australia

[4]Centre for Biomedical Technologies, Queensland University of Technology, Brisbane, QLD 4000, Australia

Corresponding authors: Ruishu Jin, ruishu.jin@data61.csiro.au; Fang-Bao Tian, fangbao.tian@unsw.edu.au

(Received 4 March 2026 UTC; revised 24 July 2026 UTC; accepted 25 July 2026 UTC)

This work investigates how spanwise twisting modulates aerodynamic performance and leading-edge vortex (LEV) dynamics of a low aspect-ratio (AR) flapping wing through variations in effective angle of attack (α_{eff}). Spanwise twisting primarily redistributes force between the streamwise and spanwise directions for a low-AR flapping wing – reallocating force orientation rather than altering total force magnitude – thereby directly governing the thrust-to-resultant-force ratio and hence propulsive efficiency. At low Strouhal number, excessive α_{eff} induces stall, while at medium-to-high Strouhal number, resultant force remains insensitive to α_{eff} as increasing twist enhances thrust at the expense of side force. Maximum propulsive efficiency of 0.36 occurs at Strouhal number $= 0.6$ and $\alpha_{eff,max} = 27°$, where the resultant force is optimally oriented in the streamwise direction, maximising the thrust-to-resultant-force ratio. Circulation analysis reveals that peak efficiency corresponds to a circulation plateau during late downstroke, sustained by a secondary structure, a lambda-shaped positive vortical structure beneath the LEV, that regulates the LEV growth. This mechanism is absent at both excessively low and high $\alpha_{eff,max}$. Spanwise vortex variations indicate functional differentiation: inboard regions maintain attached flow for lift, while outboard regions exploit LEV dynamics for thrust. Moreover, late twisting in a flapping cycle enhances efficiency by promoting vortex shedding before the stroke reversal, whereas early twisting in a flapping cycle amplifies thrust.

Key words: flow-structure interactions, swimming/flying

© The Author(s), 2026. Published by Cambridge University Press.

https://doi.org/10.1017/jfm.2026.11974 Published online by Cambridge University Press

1. Introduction

Unlike conventional fixed-wing aircraft, which are susceptible to stall at low Reynolds numbers due to the boundary layer separation under adverse pressure gradients, birds and insects achieve remarkable flight capabilities through flapping wings, demonstrating superior aerodynamic performance (Maxworthy 1981; Sane 2003; Shyy *et al.* 2008; Pesavento & Wang 2009; Liu *et al.* 2024). This flapping mechanism proves particularly effective at low to moderate Reynolds numbers, $\mathcal{O}(10^2–10^4)$, a regime where conventional fixed-wing aerodynamics becomes inefficient. Consequently, flapping-wing flight has emerged as an attractive solution for micro air vehicles (MAVs) (Ellington 1999; Wilkins & Knowles 2009; Nguyen *et al.* 2021). A deeper understanding of the force generation mechanisms in flapping wings is therefore essential for improving the performance of the MAVs.

Force generation in flapping flight arises from multiple interacting mechanisms: vortex dynamics, wing–wake interaction, wing deformation and kinematic synchronisation (Dickinson *et al.* 1999; Sane 2003; Wang 2005; Shyy *et al.* 2008; Hedrick *et al.* 2009; Chin & Lentink 2016; Bomphrey *et al.* 2017; Huang *et al.* 2023). Among these, vortical structures generated by flapping motion serve as the primary mechanism for force production, with circulation concentrated in discrete vortices rather than distributed within the boundary layer (Ford & Babinsky 2013). These structures primarily comprise the leading-edge vortex (LEV), tip vortex (TV) and trailing-edge vortex (TEV), which form through shear layer roll-up at the wing edges (Pullin & Wang 2004). The LEV plays a dominant role in force generation, contributing the majority of lift and thrust during flapping flight (Lee *et al.* 2015; Eldredge & Jones 2019), and has consequently attracted considerable research attention (Maxworthy 1979; Ellington *et al.* 1996; Videler *et al.* 2004; Muijres *et al.* 2008). Analogous LEV structures appear in the dynamic stall of helicopter blades and pitching aerofoils, where they are termed dynamic stall vortices (McCroskey 1982; Carr 1988; Mulleners & Raffel 2012; Choudhry *et al.* 2014). The evolution of these vortical structures and overall flight performance are governed by several non-dimensional parameters, including Reynolds number, reduced frequency, Strouhal number and effective angle of attack (Shyy & Liu 2007; Platzer *et al.* 2008; Shyy *et al.* 2010; Young *et al.* 2014). Among these, the effective angle of attack has emerged as particularly critical for LEV stability and thrust production (Hover *et al.* 2004; Schouveiler *et al.* 2005; Baik *et al.* 2012).

While these aerodynamic mechanisms are fundamental to force generation, they are intrinsically coupled with structural dynamics, creating complex fluid–structure interactions at the intersection of aerodynamics and biomechanics. Both insects and birds exploit wing deformation to enhance flight performance, though through fundamentally different control strategies (Young *et al.* 2009; Du & Sun 2010; Phan & Park 2020). Birds actively modulate wing shape through musculoskeletal control, whereas insects rely predominantly on passive deformation arising from their wings' inherent flexibility (Wootton 1992; Walker *et al.* 2009). This passive deformation, driven by aerodynamic loading, plays a crucial role in force generation and flight stability (Wootton 1993; Mountcastle & Combes 2013). Similar passive mechanisms operate in avian flight, where structures such as the alula and covert feathers deform in response to local flow conditions, enhancing aerodynamic performance (Carruthers *et al.* 2007; Walker *et al.* 2012). Experimental investigations have demonstrated that flapping wings can generate controlled aerodynamic forces through stable leading-edge vorticity, with trailing-edge flexibility serving as a key parameter in force modulation (Zhao *et al.* 2010). To complement these

https://doi.org/10.1017/jfm.2026.11974 Published online by Cambridge University Press

experimental insights and probe the detailed flow physics, computational fluid dynamics (CFD) has emerged as a promising tool for elucidating these complex fluid–structure interactions. Nakata & Liu (2012) developed a comprehensive numerical framework for simulating flexible-wing insect flight, validating their approach through benchmark tests and detailed hawkmoth flight analysis. Subsequent numerical studies have demonstrated that wing flexibility can significantly enhance aerodynamic efficiency across various flapping configurations (Shoele & Zhu 2013; Zhu *et al.* 2014; Shahzad *et al.* 2018; Addo-Akoto *et al.* 2021).

Active wing twisting has been shown to achieve higher propulsive efficiency compared with passive deformation (Mackenzie 2012). Analogous to propeller blades, flapping wings employ spanwise twist from root to tip to modulate the effective angle of attack distribution and prevent stall (McGahan 1973; Norberg 1990). Despite its aerodynamic significance, the underlying mechanisms through which wing twisting enhances flight performance remain incompletely understood. While several studies have examined the effects of active twisting on force generation and vortex dynamics, significant knowledge gaps persist. Thielicke & Stamhuis (2018) investigated force generation through indirect measurements, but left the relationship between twist kinematics and LEV evolution largely unexplored. The distinct aerodynamic roles of the inner and outer wing sections during twisted flapping motion also remain unclear (Thielicke & Stamhuis 2015). Recent investigations have provided additional insights, for example, aspect-ratio effects in rolling and twisting aerofoils (Zurman-Nasution *et al.* 2021), in which the strong spanwise flows in the low aspect-ratio wing could stabilise the LEV, and the role of chordwise deformation in batoid fish propulsion, where asymmetric fin motion optimises thrust through controlled vortex dynamics (Zhang *et al.* 2022*a*). Nevertheless, the fundamental mechanisms linking twist-induced angle of attack modulation to propulsive performance require further investigation.

An unresolved question in flapping-wing aerodynamics is whether an optimal spanwise distribution of effective angle of attack exists for maximising propulsive performance (Thielicke & Stamhuis 2018). While numerous studies suggest that spanwise twisting enables birds to achieve superior aerodynamic efficiency through favourable effective angle of attack distributions (Thomas & Hedenström 1998; Alexander 2002; Hubel 2007; Azuma 2012), the underlying flow physics remain unexplored (Usherwood & Ellington 2002). This study addresses these knowledge gaps through systematic investigation of how spanwise twist affects aerodynamic performance in flapping flight. Specifically, we examine the relationship between twist kinematics and propulsive force generation, efficiency and LEV dynamics. Our objectives are threefold: first, to identify optimal effective angle of attack distributions and quantify their impact on propulsive efficiency; second, to elucidate the physical mechanisms through which twist modulation enhances performance via altered LEV evolution; and third, to characterise the distinct aerodynamic roles of the inner and outer wing sections during twisted flapping motion. The findings of the present study have potential implications for the design of flapping-wing micro air vehicles, where spanwise modulation of the effective angle of attack could be exploited to enhance aerodynamic performance (Zhang *et al.* 2022*b*; Rafee Nekoo *et al.* 2025; Wu *et al.* 2026).

The remainder of this paper is organised as follows. Section 2 introduces the physical model and numerical methods. Results and their discussion are presented in § 3 and conclusions are drawn in § 4.

https://doi.org/10.1017/jfm.2026.11974 Published online by Cambridge University Press

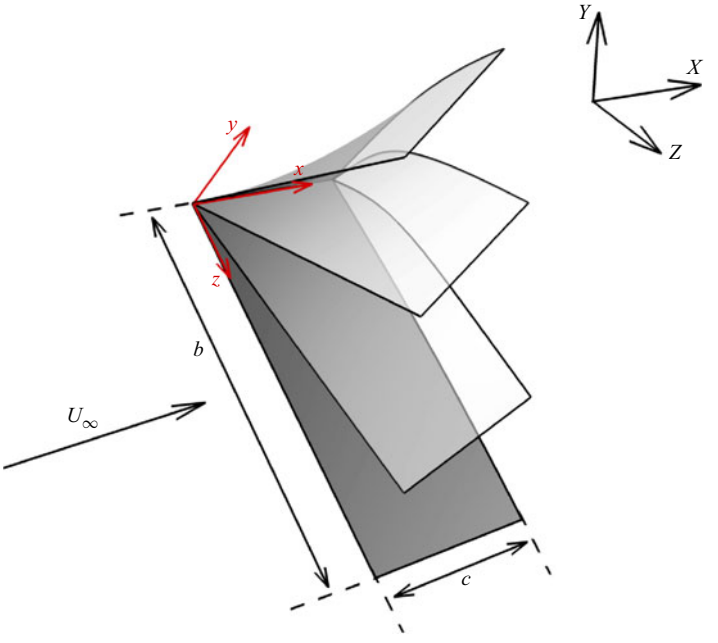


Figure 1. A rectangular flat-plate wing making a flapping motion about the x axis and a twisting motion from the root to the tip about the z axis.

2. Physical model and methodologies

2.1. *Physical model and governing equations*

A thin rectangular flat-plate wing is flapping down about the x axis and twisting about the z axis, as shown in figure 1, where the translucent areas represent the wings at earlier times during the flapping down period. The global axis orientation is XYZ, while the moving reference frame attached to the leading edge is xyz in red. Here, U_∞ denotes the constant freestream velocity, c is the wing chord length and b is the spanwise length. The practical bird wing is simplified to a thin, rectangular, flat-plate wing in simulations as the wing thickness and the leading-edge geometry have been shown to have limited effects on the aerodynamic performance and the LEV dynamics for flapping wings (Rival *et al.* 2014; Thielicke & Stamhuis 2015). In this work, c and b are set to be 1 and 3, respectively, leading to the aspect ratio (AR) of 3, which is within the range of the AR of small birds (Tobalske & Dial 1996; Azuma 2012). Although varying the wing AR leads to distinct aerodynamic performance and vortex dynamics (Harbig *et al.* 2013; Fu *et al.* 2014; Han *et al.* 2015; Phillips *et al.* 2015), a qualitatively similar vortex system development has been observed across the range $1 \leqslant AR \leqslant 4$ for rotating wings (Garmann & Visbal 2014). Furthermore, most natural flyers possess low-aspect-ratio wings, which has been attributed to two key mechanisms: the avoidance of LEV burst (Fu *et al.* 2014) and the constraint imposed by the chord length on the LEV circulation growth (Garmann & Visbal 2014). In light of these considerations, an aspect ratio of $AR = 3$ is adopted in the present study, striking a balance between physical relevance and the need to maintain a tractable parameter space and manageable computational cost.

The flapping kinematics is defined by the flapping angle about the x axis $\phi(t)$, the prescribed effective angle of attack $\alpha_{eff}(t, z)$ and the twisting motion about the z axis (the leading edge) from the wing root to the wing tip is defined by $\Theta(t, z)$. Here, $\phi(t)$ is

https://doi.org/10.1017/jfm.2026.11974 Published online by Cambridge University Press

defined first as

$$\phi(t) = \phi_0 \cos(2\pi f t), \tag{2.1}$$

where ϕ_0 is the amplitude of the flapping angle, f is the flapping frequency. The ϕ_0 is set to be 0.559 (32°) according to the flapping angle of small birds during cruise (Rosén *et al.* 2004). Additionally, f varies according to the Strouhal number, $St_A = f(2\phi_0 b)/U_\infty$ from 0.4 to 1.0 with an increment of 0.1, in which $(2\phi_0 b)$ is the arc length of the wing tip trajectory caused by $\phi(t)$. It should be noted that St_A in this work is evaluated based on the flapping amplitude of the wing tip. However, if re-evaluated using the displacement of the wing mid-section (i.e. the average displacement from root to tip), the St_A range would cover that observed in birds during efficient cruising flight (Taylor *et al.* 2003), 0.2–0.4. Taylor *et al.* (2003) modelled the wing as undergoing purely heaving motion, rather than flapping about an axis.

The effective angle of attack induced by the flapping motion $\phi(t)$ at each wing section can be calculated as

$$\alpha_{eff,\phi}(t, z) = \arctan[\dot{\phi}(t)(z - z_{root})/U_\infty], \tag{2.2}$$

where z_{root} is the coordinate of the base of the flapping wing and $z \geqslant z_{root}$. For a bird, the range of the maximum effective angle of attack at the wing tip, $\alpha_{eff,max}$, is from 9° to 54° according to the previous studies and observations on birds (McGahan 1973; Pennycuick 1989; Thomas & Hedenström 1998; Usherwood & Ellington 2002; Azuma 2012). Therefore, the effective angle of attack at each wing section, $\alpha_{eff}(t, z)$, is prescribed by the following equation in the simulations:

$$\alpha_{eff}(t, z) = \alpha_{eff,max}(z - z_{root}) \cos(2\pi f t - \pi/2 + \Phi)/b, \tag{2.3}$$

on which the linear variation along the spanwise direction is assumed. Here, Φ is the phase difference between $\alpha_{eff}(t, z)$ and $\phi(t)$. For this flapping wing, the effective angle of attack is the result of the flapping motion $\phi(t)$ and the twisting motion $\Theta(t, z)$. The twisting motion is equivalent to a pitching down (up) motion for each spanwise wing section during the flapping down (up) period. Thus, the twisting angle can be evaluated by the following equation:

$$\Theta(t, z) = \alpha_{eff,\phi}(t, z) - \alpha_{eff}(t, z). \tag{2.4}$$

To demonstrate the variation in the effective angle of attack along the wing span, the time histories of α_{eff} at three spanwise locations are shown in figure 2. It can be seen that the twisting motion is superposed onto the flapping motion to maintain α_{eff} in a reasonable range in a flapping cycle.

The flow dynamics is governed by the incompressible Navier–Stokes equations due to the small Mach number of birds and MAV applications:

$$\nabla \cdot \boldsymbol{u} = 0, \tag{2.5a}$$

$$\frac{\partial \boldsymbol{u}}{\partial t} + \boldsymbol{u} \cdot \nabla \boldsymbol{u} = -\nabla p + \frac{1}{Re}\nabla^2 \boldsymbol{u} + \boldsymbol{f}, \tag{2.5b}$$

where $\boldsymbol{u}$ is the dimensionless velocity, p is the dimensionless pressure, $\boldsymbol{f}$ is the dimensionless body force density and Re is the Reynolds number defined as $Re = U_\infty c/\nu$ with ν being the kinematic viscosity.

2.2. *Numerical methods*

To solve the flow dynamics, we employ the lattice Boltzmann method (LBM) coupled with a feedback immersed boundary method (IBM) because of its high computational

https://doi.org/10.1017/jfm.2026.11974 Published online by Cambridge University Press

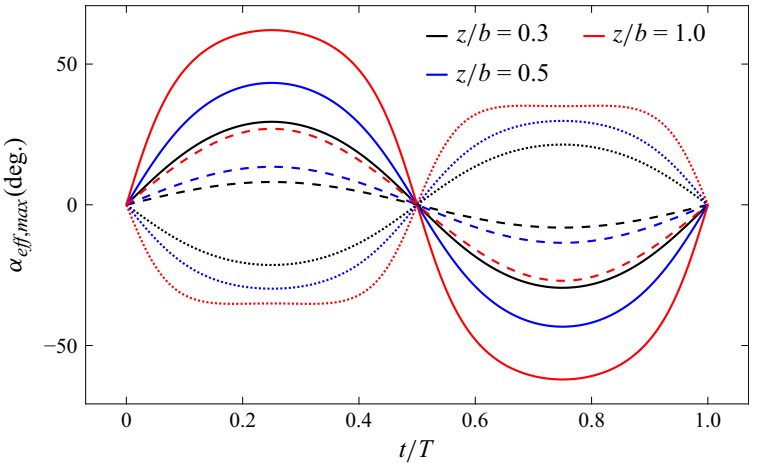


Figure 2. Time histories of α_{eff} at spanwise locations $z/b = 0.3$, 0.5 and 1.0 during a complete flapping cycle at $St_A = 0.6$, $\alpha_{eff,max} = 27°$ and $\Phi = 0°$. Solid lines, dash lines and dotted lines represent α_{eff} induced by the flapping motion, the prescribed α_{eff} and α_{eff} due to the twisting motion, respectively.

efficiency and straightforward implementation (Chen & Doolen 1998; Aidun & Clausen 2010; Krüger *et al.* 2017). The LBM solves the discrete lattice Boltzmann equation with the D3Q19 lattice model (three-dimensional model with 19 discrete velocity directions),

$$f_i(\boldsymbol{x} + \boldsymbol{e}_i \Delta t, t + \Delta t) - f_i(\boldsymbol{x}, t) = \Omega_i + \Delta t G_i. \tag{2.6}$$

The evolution of the particle distribution function, $f_i(\boldsymbol{x}, t)$, with the discrete lattice velocity vector, $\boldsymbol{e_i}$, is determined by the collision function, Ω_i, and the external source term, G_i, due to the external body force from the immersed boundary object. The fluid density, pressure and velocity can respectively be evaluated from the moments of f_i according to the following equations:

$$\rho = \sum_i f_i, \quad p = \rho c_s^2 \quad \text{and} \quad \boldsymbol{u} = \left(\sum_i \boldsymbol{e}_i f_i + \frac{1}{2} \boldsymbol{f} \Delta t \right) \Big/ \rho, \tag{2.7}$$

where $c_s = \Delta x/(\Delta t\sqrt{3})$ is the ideal sound speed in the LBM model. Here, Ω_i and G_i are the recursive regularised collision model (Coreixas *et al.* 2017) and the source scheme proposed by Guo *et al.* (2002), respectively:

$$\Omega_i(\boldsymbol{x}, t) = \frac{1}{\tau} f_i^{(1)}, \tag{2.8}$$

$$G_i = \left(1 - \frac{1}{2\tau}\right) \omega_i \left(\frac{\boldsymbol{e}_i - \boldsymbol{u}}{c_s^2} + \frac{\boldsymbol{e}_i \cdot \boldsymbol{u}}{c_s^4} \boldsymbol{e}_i \right) \cdot \boldsymbol{f}, \tag{2.9}$$

where τ is the dimensionless relaxation time defined as $\tau = \nu/(c_s^2 \Delta t) + 1/2$, $f_i^{(1)}$ is the non-equilibrium part of the particle distribution function f_i from the recursive regularised procedure (Latt & Chopard 2006; Coreixas *et al.* 2017) and ω_i is the weighted coefficient of the D3Q19 model. To avoid duplication and verbosity, the formulation of equilibrium ($f_i^{(eq)}$) and non-equilibrium ($f_i^{(1)}$) distribution components in the recursive regularised scheme follows the paper of Coreixas *et al.* (2017).

For the wing boundary conditions, we adopt a feedback IBM, which offers straightforward treatment of moving complex geometrical configurations (Goldstein *et al.* 1993;

https://doi.org/10.1017/jfm.2026.11974 Published online by Cambridge University Press

Peskin 2002; Mittal & Iaccarino 2005; Huang & Tian 2019; Griffith & Patankar 2020). Specifically, a body force is applied near the wing to achieve the no-slip boundary condition:

$$\boldsymbol{f} = -\int \boldsymbol{F}(\boldsymbol{s}, t)\delta(\boldsymbol{x} - \boldsymbol{X}(\boldsymbol{s}, t))\,\mathrm{d}A, \tag{2.10}$$

where $\boldsymbol{s}$ denotes the curvilinear coordinates attached to the structure element, $\boldsymbol{X}(\boldsymbol{s}, t)$ represents its position at time t and $\boldsymbol{F}(\boldsymbol{s}, t)$ is the Lagrangian force acting on the structure. The terms $\mathrm{d}A$ and δ denote the surface area element and the Dirac delta function, respectively. Here, $\boldsymbol{F}(\boldsymbol{s}, t)$ is evaluated by the feedback scheme:

$$\boldsymbol{F} = \beta(\boldsymbol{U}_{ib}(\boldsymbol{s}, t) - \boldsymbol{U}(\boldsymbol{s}, t)), \tag{2.11a}$$

$$\boldsymbol{U}_{ib}(\boldsymbol{s}, t) = \int \boldsymbol{u}(\boldsymbol{x}, t)\delta(\boldsymbol{x} - \boldsymbol{X}(\boldsymbol{s}, t))\,\mathrm{d}\boldsymbol{x}, \tag{2.11b}$$

where $\boldsymbol{U}_{ib}(\boldsymbol{s}, t)$ and $\boldsymbol{U}(\boldsymbol{s}, t)$ denote the fluid velocity interpolated onto the structure element from the surrounding fluid and the actual velocity of the structure element, respectively, while β is the feedback coefficient. Following Huang *et al.* (2022), the feedback coefficient is set to $\beta = 2.6$ in LBM units. The Dirac delta function $\delta(\boldsymbol{x})$ is approximated by the smoothed delta function $\delta_h(\boldsymbol{x})$ proposed by Peskin (2002):

$$\delta_h(\boldsymbol{x}) = \frac{1}{\Delta x \Delta y \Delta z}\phi_r\left(\frac{x}{\Delta x}\right)\phi_r\left(\frac{y}{\Delta y}\right)\phi_r\left(\frac{z}{\Delta z}\right), \tag{2.12a}$$

$$\phi_r(r) = \begin{cases} \dfrac{1}{8}\left(3 - 2|r| + \sqrt{1 + 4|r| - 4r^2}\right), & 0 \leqslant |r| < 1, \\ \dfrac{1}{8}\left(5 - 2|r| - \sqrt{-7 + 12|r| - 4r^2}\right), & 1 \leqslant |r| < 2, \\ 0, & |r| \geqslant 2. \end{cases} \tag{2.12b}$$

The implementation and validation of the immersed boundary-lattice Boltzmann method solver have been thoroughly documented in our previous work works (Jin *et al.* 2024, 2025; Wang *et al.* 2024).

2.3. *Simulation set-up*

As shown in figure 3, a multi-block mesh is employed to improve the computational efficiency and accuracy, where the finer mesh is applied near the wing to resolve the small scales and the coarse blocks with a coarsening ratio of 2 are applied away from the wing to reduce the computational expense. The computational domain spans from $(-15c, -15c, -15c)$ to $(30c, 15c, 15c)$ in the X, Y and Z directions. The velocity boundary condition, $\boldsymbol{u} = (U_\infty, 0, 0)$, and the zero gradient pressure boundary condition, $\nabla p = 0$, are applied on the boundaries of the domain except for the outlet surface $(X = 30c)$, on which the zero gradient velocity boundary condition and the constant pressure boundary condition are applied. The absorbing layers are applied on the lattices near the boundaries of the domain to reduce the effects of the reflecting acoustic waves (Xu & Sagaut 2013). The simulations are run for five flapping cycles to achieve a steady state and results in the fifth flapping cycle are used to conduct analysis.

https://doi.org/10.1017/jfm.2026.11974 Published online by Cambridge University Press

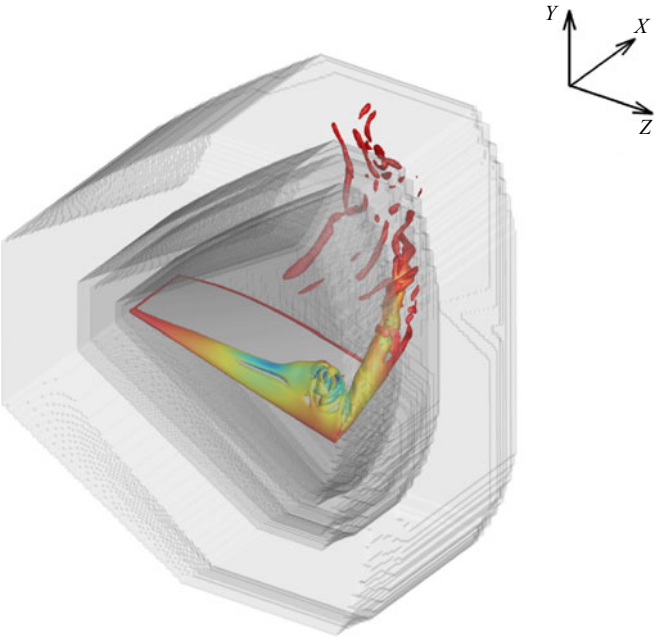


Figure 3. A top-port view of the finest three mesh blocks.

To measure the flying performance of the flapping wing, the thrust, lift, side force, resultant force magnitude and power consumption coefficients are defined as follows:

$$C_T = \frac{-F_x}{1/2\rho_0 A U_\infty^2}, \quad C_L = \frac{F_y}{1/2\rho_0 A U_\infty^2}, \quad C_Z = \frac{F_z}{1/2\rho_0 A U_\infty^2}, \quad C_F = \frac{|\boldsymbol{F}|}{1/2\rho_0 A U_\infty^2},$$
$$C_P = \frac{\int \boldsymbol{F}\cdot\boldsymbol{U}\,\mathrm{d}\boldsymbol{A}}{1/2\rho_0 A U_\infty^3}, \tag{2.13}$$

where F_x, F_y and F_z are the force components on the flapping wing in the $+X$, $+Y$ and $+Z$ directions, respectively. Here, A is the integration of $\mathrm{d}A$ over the structural triangle elements. The wing area change due to the twisting is presented in Appendix A.2 to demonstrate that the change of the wing area is very small.

The propulsive efficiency is defined as follows:

$$\eta = \frac{\overline{C_T} U_\infty}{\overline{C_P}}. \tag{2.14}$$

To ensure the convergence of the simulation results, the mesh-dependence studies are conducted at $Re = 4500$, as shown in Appendix A.3. At $Re = 4500$, the Vreman sub-grid stress model (Vreman 2004) is adopted in the large eddy simulation due to its satisfactory balance in efficiency and accuracy. The effects of Re are documented in Appendix A.1 by simulations at $Re = 500$ and 4500. It is found that the effects of Re are limited, which are consistent with the previous work on flapping wings (Anderson *et al.* 1998; Bozkurttas *et al.* 2009; Zhang *et al.* 2018). Therefore, the results and discussions are conducted according to the simulations at $Re = 1500$.

https://doi.org/10.1017/jfm.2026.11974 Published online by Cambridge University Press

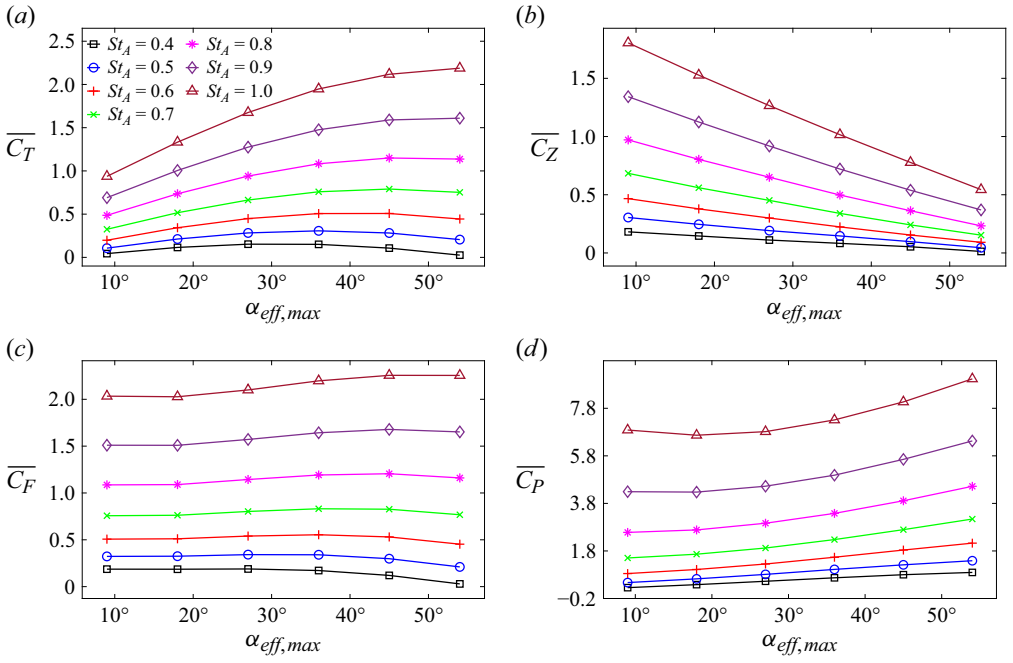


Figure 4. Cycle-average aerodynamic performance coefficients at $Re = 1500$: (*a*) thrust coefficient; (*b*) side force coefficient; (*c*) resultant force magnitude coefficient and (*d*) power consumption coefficients.

3. Results and discussions

The effects of St_A and $\alpha_{eff,max}$ are investigated first to identify the most efficient combination of St_A and $\alpha_{eff,max}$ by fixing $\Phi = 0°$. Then, the effects of Φ are investigated by varying it from $-40°$ to $40°$ with an increment of $10°$.

3.1. *Optimal α_{eff} and St_A*

The cycle-averaged force production is first analysed to reveal the effects of St_A and $\alpha_{eff,max}$ on force generation. Figure 4 presents the cycle-averaged force coefficients as functions of these parameters. As expected, all force coefficients and mechanical power consumption increase monotonically with St_A, which is attributable to the higher flapping frequency. In contrast, the response to variations in $\alpha_{eff,max}$ is more complex and reveals several important aerodynamic characteristics. First, the cycle-averaged thrust coefficient $\overline{C_T}$ (figure 4*a*) exhibits qualitatively different behaviours depending on St_A. At low Strouhal numbers ($St_A \leqslant 0.6$), $\overline{C_T}$ initially increases with $\alpha_{eff,max}$ before declining at higher angles, indicating an optimal effective angle of attack for thrust generation. Conversely, at high Strouhal numbers ($St_A > 0.6$), thrust increases monotonically with $\alpha_{eff,max}$. This suggests that excessive effective angles of attack are detrimental to thrust generation in the low-to-medium St_A regime – characteristic of typical avian cruising flight. Consequently, maintaining an appropriate spanwise distribution of effective angle of attack is crucial for optimal flight performance. Second, the cycle-averaged side force coefficient $\overline{C_Z}$ (figure 4*b*) decreases monotonically with increasing $\alpha_{eff,max}$, exhibiting a trend opposite to that of $\overline{C_T}$ at high St_A. This inverse relationship suggests a trade-off between thrust and side force generation as the effective angle of attack is modulated through wing twist. Third, the cycle-averaged resultant force magnitude coefficient $\overline{C_F}$ (figure 4*c*) remains relatively insensitive to $\alpha_{eff,max}$ across all Strouhal numbers examined, suggesting that the

https://doi.org/10.1017/jfm.2026.11974 Published online by Cambridge University Press

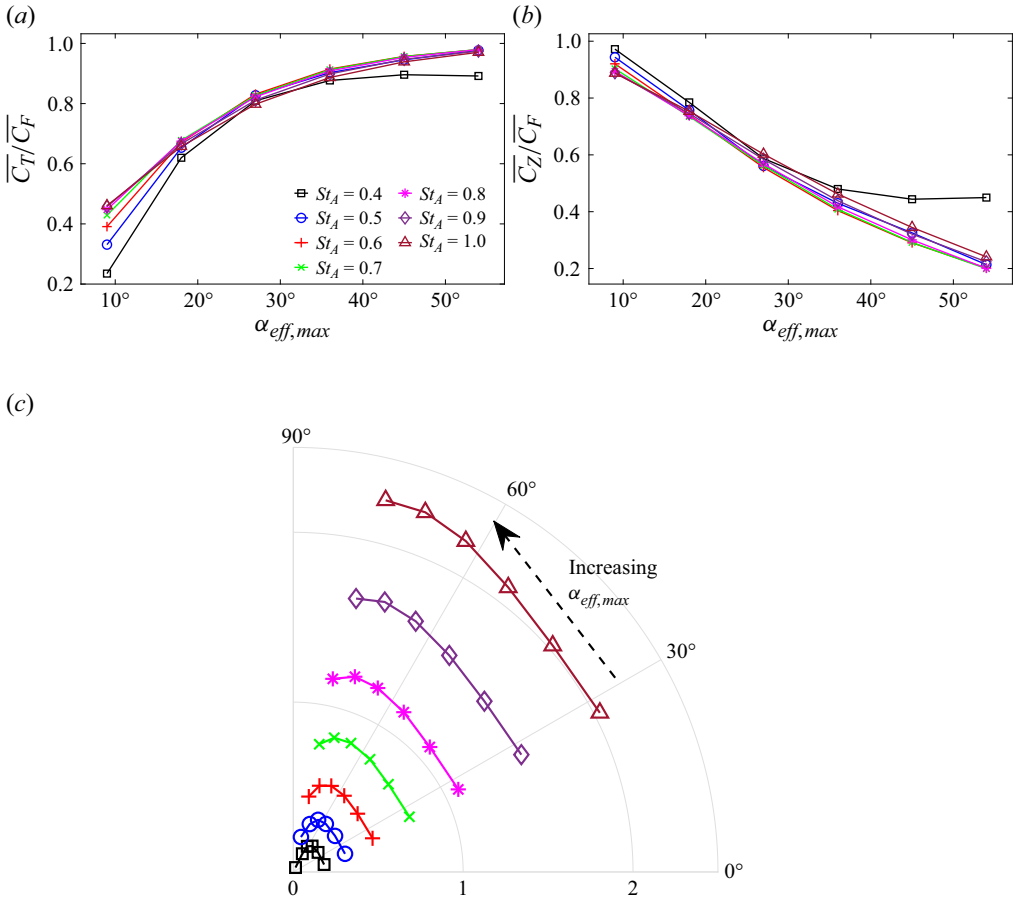


Figure 5. Average (a) thrust and (b) side force coefficients normalised by the average resultant force magnitude coefficient at $Re = 1500$. (c) Magnitude (radius) and the direction (azimuth angle) of the cycle-averaged resultant force magnitude coefficient at $Re = 1500$. The X direction is along the 90° direction and the Z direction is along the 0° direction. The increase direction of $\alpha_{eff,max}$ is indicated by the arrow.

magnitude of the total aerodynamic force is governed primarily by St_A rather than by twist kinematics. Finally, the cycle-averaged power consumption coefficient $\overline{C_P}$ (figure 4d) increases with $\alpha_{eff,max}$ for all cases. Notably, this increase is approximately linear for intermediate Strouhal numbers ($St_A = 0.4$–0.6), while higher St_A cases exhibit accelerated power consumption at large $\alpha_{eff,max}$. Moreover, combining observations from figures 4(a) and 4(d) reveals an optimal $\alpha_{eff,max}$ for propulsive efficiency. Notably, thrust exhibits a sub-linear scaling with $\alpha_{eff,max}$ (power-law exponent <1), whereas power consumption scales super-linearly (power-law exponent >1). This disparity in scaling behaviours implies that propulsive efficiency necessarily reaches a maximum at moderate $\alpha_{eff,max}$, beyond which the rapidly increasing power penalty outweighs the diminishing thrust gains.

As demonstrated in figure 4, the effect of St_A is straightforward: larger St_A yields greater force coefficients and mechanical power consumption. The effect of $\alpha_{eff,max}$ – which reflects the influence of spanwise twisting – is now examined in detail. Figure 5 presents the cycle-averaged thrust and side force coefficients normalised by the resultant force magnitude coefficient. Remarkably, all curves collapse onto a single trend, except for $St_A = 0.4$, which exhibits relatively larger deviations at low and high $\alpha_{eff,max}$.

https://doi.org/10.1017/jfm.2026.11974 Published online by Cambridge University Press

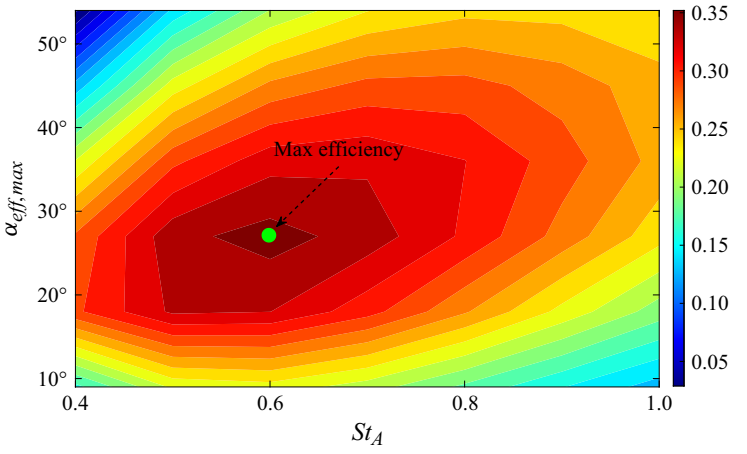


Figure 6. Contour of the propulsive efficiency, η, on the St_A–$\alpha_{eff,max}$ plane at $Re = 1500$.

This collapse reveals that spanwise twisting primarily reallocates force production between the streamwise and spanwise directions rather than altering the total force magnitude. At low $\alpha_{eff,max}$ (corresponding to significant spanwise twisting), force production is predominantly oriented in the spanwise direction. Conversely, at high $\alpha_{eff,max}$ (corresponding to minor spanwise twisting), force production shifts predominantly to the streamwise direction, thereby generating thrust.

The magnitude and direction of the resultant force magnitude coefficient are shown in figure 5(c), where 0° corresponds to the $+Z$ direction and 90° corresponds to the streamwise direction, $+X$. Two important observations emerge from this analysis. First, the force direction is primarily governed by $\alpha_{eff,max}$. As $\alpha_{eff,max}$ increases (less twist), the resultant force vector rotates from $+Z$ to the streamwise direction. This behaviour elucidates the underlying mechanism of force reallocation observed in figures 5(a) and 5(b). Second, at low flapping frequencies, stall occurs when $\alpha_{eff,max}$ becomes excessively large, as evidenced by the rapid decrease in $\overline{C_F}$. While stall on stationary wings is well documented when the angle of attack exceeds a critical value, the present results demonstrate that stall can also occur on flapping wings when the spanwise distribution of α_{eff} is inappropriate. This finding underscores the importance of proper spanwise twisting in both preventing stall and maintaining efficient force production.

Figure 6 shows the propulsive efficiency in the St_A–$\alpha_{eff,max}$ parameter space. A maximum efficiency of $\eta = 0.36$ is attained at $St_A = 0.6$ and $\alpha_{eff,max} = 27°$. This optimal condition exhibits two noteworthy characteristics. First, the Strouhal number based on mid-span amplitude (rather than wing-tip amplitude) is $St_A = 0.3$, consistent with the range observed for efficient avian cruise (Taylor *et al.* 2003). Second, the spanwise-averaged effective angle of attack is $\alpha_{eff} = 13.5°$, which closely matches the optimal value of 15° reported for two-dimensional heaving and pitching aerofoils (Schouveiler *et al.* 2005).

3.2. *Analysis on the instantaneous flow field*

The preceding analysis has established that St_A primarily governs the magnitude of force production, while spanwise twisting redistributes this force between the streamwise and spanwise directions. This section examines the instantaneous force production and associated vortex dynamics at the optimal efficiency condition of $St_A = 0.6$. Figure 7

https://doi.org/10.1017/jfm.2026.11974 Published online by Cambridge University Press

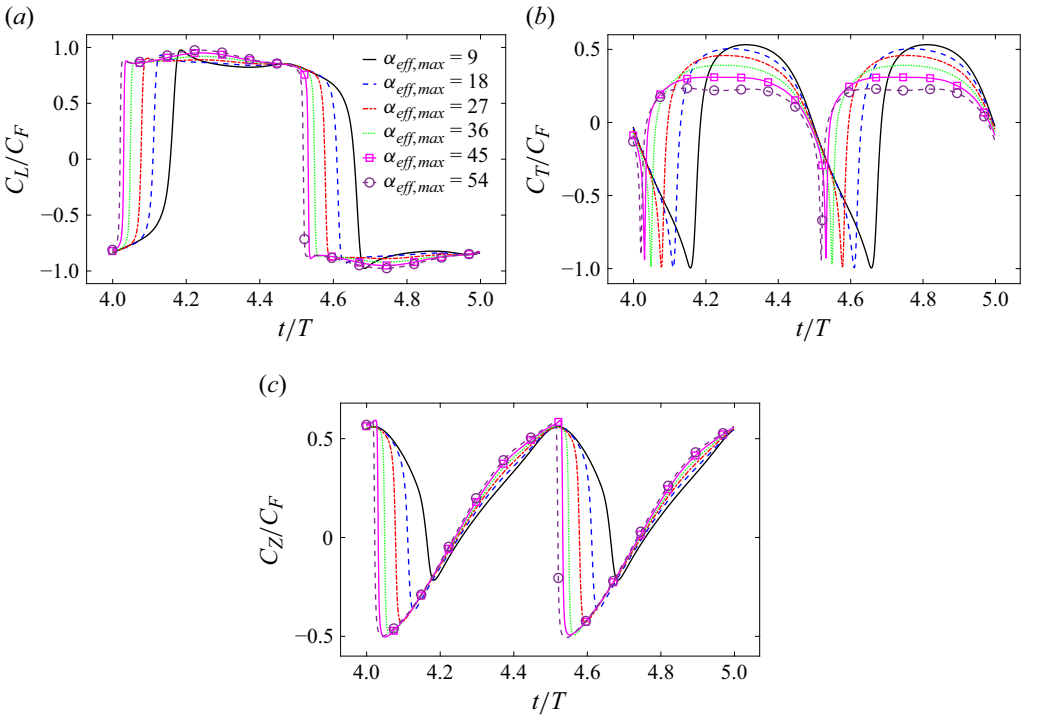


Figure 7. Instantaneous (*a*) lift, (*b*) thrust and (*c*) side force coefficients normalised by the resultant force magnitude coefficient at $St_A = 0.6$ and $Re = 1500$.

presents the time histories of the instantaneous lift, thrust and side force coefficients normalised by the magnitude of the resultant force coefficient, which are defined in (2.13) of § 2.3. Three key features emerge from this analysis. First, owing to the flapping motion being symmetric about the XZ plane, the net lift production is zero over a complete cycle (figure 7*a*). However, spanwise twisting influences the instantaneous lift generation: as the twisting magnitude increases ($\alpha_{eff,max}$ decreases), the lift production phase is delayed within the flapping cycle. Second, the normalised thrust coefficient C_T/C_F (figure 7*b*) exhibits two trends with increasing spanwise twisting: the magnitude of C_T/C_F increases, while the duration of thrust production decreases. Third, the normalised side force coefficient C_Z/C_F (figure 7*c*) shows that increasing spanwise twisting reduces side force production in the $-Z$ direction and delays the timing at which C_Z reaches its negative peak.

The influence of spanwise twisting on vortex structures is now examined. Figure 8 presents three-dimensional flow structures visualised using iso-surfaces of the Q-criterion (Jeong & Hussain 1995) and coloured by the pressure coefficient, $C_p = (p - p_\infty)/(1/2\rho U_\infty^2)$, at $St_A = 0.6$ for $\alpha_{eff,max} = 9°$, 27° and 45°. These configurations correspond to the conditions yielding maximum side force, maximum propulsive efficiency and maximum thrust, respectively, at $St_A = 0.6$. At the beginning of the downstroke ($t/T = 4.125$), the shear layer rolls up into a leading-edge vortex (LEV) at the outer wing region for all cases, driven by flow separation at the sharp leading edge. For $\alpha_{eff,max} = 9°$, LEV formation is less pronounced compared with higher $\alpha_{eff,max}$ cases; the LEV does not appear to pinch off from its downstream boundary layer due to the small effective angle of attack (Akkala & Buchholz 2017). In contrast, a tip vortex (TV) is evident for $\alpha_{eff,max} = 27°$ and 45° at this instant. At $\alpha_{eff,max} = 45°$, the pressure within

https://doi.org/10.1017/jfm.2026.11974 Published online by Cambridge University Press

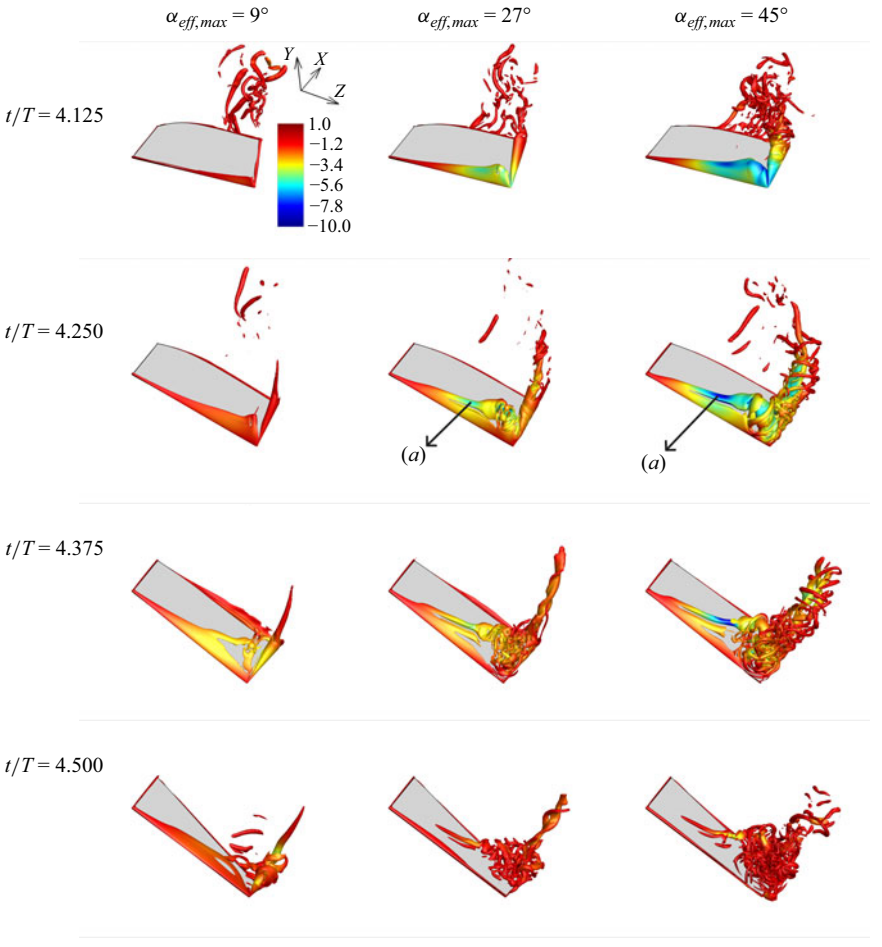


Figure 8. The three-dimensional (3-D) vortical structures identified by $Q = 50$ coloured by the pressure coefficient at $St_A = 0.6$ and $\alpha_{eff,max} = 9°, 27°, 45°$ in the fifth flapping cycle.

both the LEV and TV is substantially lower than at smaller $\alpha_{eff,max}$, indicating stronger circulation. By $t/T = 4.250$, a low-pressure LEV tube (refer to feature (a)) oriented in the spanwise direction $(+z)$ develops for $\alpha_{eff,max} = 27°$ and 45°, with the LEV also tilting in the streamwise direction $(+x)$. For $\alpha_{eff,max} = 9°$, the LEV remains weak and its core pressure is considerably higher than in the other two cases, resulting in substantially reduced thrust production. Notably, vortex breakdown occurs at the outer wing region (approximately $z/b = 0.7$) for $\alpha_{eff,max} = 27°$ and 45°, where the LEV cross-sectional area increases abruptly – a phenomenon similar to that observed on rotating wings (Medina & Jones 2016). Following breakdown, the LEV core can no longer sustain low pressure. At $\alpha_{eff,max} = 45°$, additional small-scale structures emerge around the TV owing to the higher local Reynolds number of the shear layer feeding these vortical structures. At $t/T = 4.375$, the LEV over the outer wing region loses coherence and detaches from the surface for $\alpha_{eff,max} = 27°$ and 45°. However, the low-pressure LEV tube over the mid-span region remains attached, indicating that the LEV from root to mid-span continues to generate suction force. Finally, at the end of the downstroke ($t/T = 4.500$), the LEV fully detaches from the wing surface due to wing rotation at the onset of the upstroke.

https://doi.org/10.1017/jfm.2026.11974 Published online by Cambridge University Press

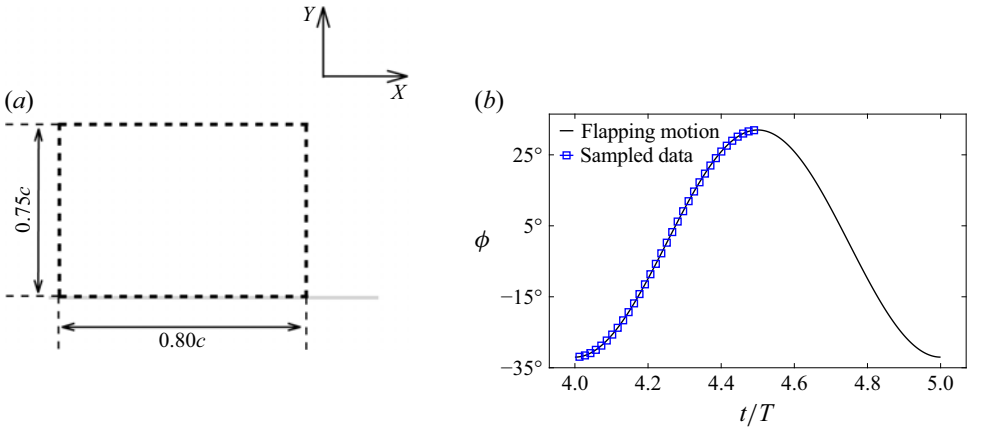


Figure 9. Sectional LEV circulation analysis along the wing span. (*a*) Control volume at a specific spanwise location represented in the local sectional reference frame. (*b*) Sampled data during the downstroke period.

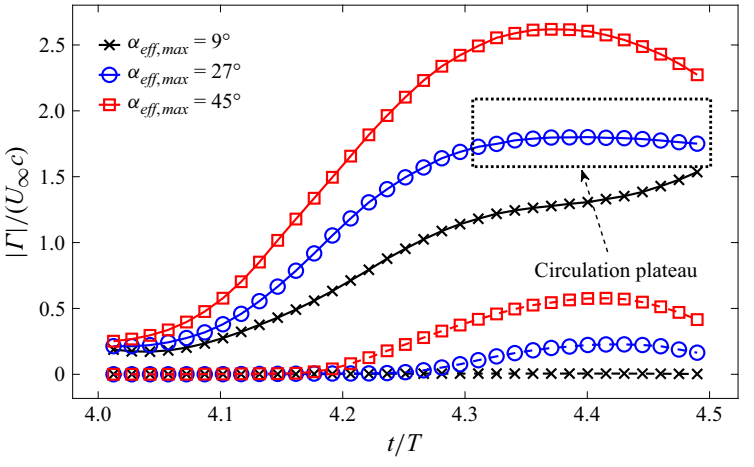


Figure 10. Temporal evolution of the circulations of the LEV and the secondary structure at $z/b = 0.6$. The solid lines represent the LEV (negative vorticity) and the dashed lines represent the secondary structure (positive vorticity).

The sectional LEV circulation analysis is conducted at two spanwise locations, $z/b = 0.3$ and 0.5, to investigate the effects of $\alpha_{eff,max}$ on the development of the LEV at $St_A = 0.6$, and $\alpha_{eff,max} = 9°$, 27° and 45°. As shown in figure 9(*a*), a local control volume is placed on the top of the suction side of the wing, which is aligned with the local wing chordwise direction. The control volume extends from $0.05c$ to $0.85c$ in the chordwise direction and $0c$ to $0.75c$ in the chord-normal direction, where the LEV is fully contained during the whole downstroke period. As shown in figure 9(*b*), the circulation of the cross-sections of the LEV at three spanwise locations is recorded at 33 instances during the downstroke period.

The temporal evolution of circulation and vorticity contours of the LEV at the mid-span locations ($z/b = 0.6$) are presented in figures 10 and 11, respectively. The circulation is the integration of the vorticity field in the control volume. Three representative time instants are shown for each $\alpha_{eff,max}$ in figure 11, revealing distinct vortex dynamics depending on the degree of spanwise twisting. Figure 10 shows that for $\alpha_{eff,max} = 27°$, the LEV

https://doi.org/10.1017/jfm.2026.11974 Published online by Cambridge University Press

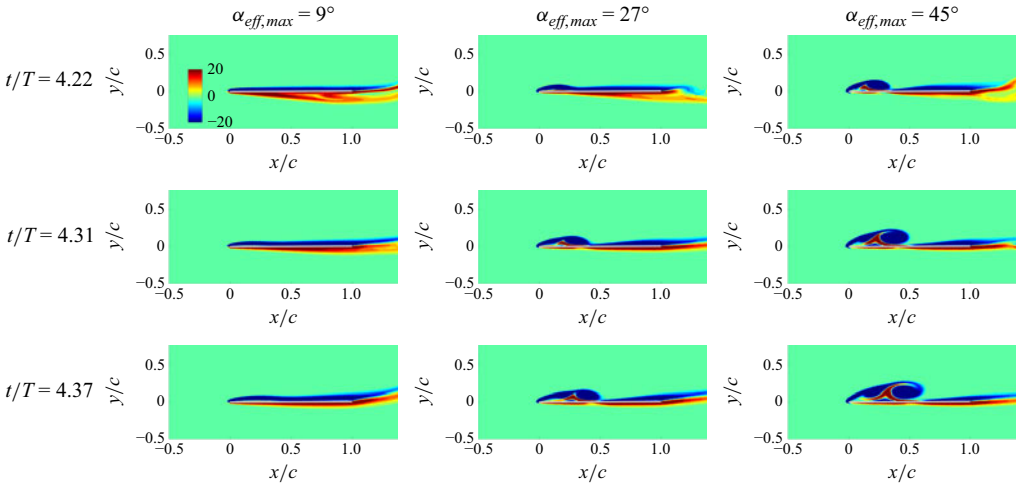


Figure 11. Vorticity contour of the LEV cross-section at $z/b = 0.6$.

circulation exhibits a plateau region, characteristic of a well-regulated vortex growth mechanism. In contrast, at $\alpha_{eff,max} = 9°$, the LEV circulation increases monotonically (roughly linearly) throughout the downstroke without reaching a peak. The vorticity contours in figure 11 confirm that the LEV does not pinch off from its downstream boundary layer at this low effective angle of attack. At $\alpha_{eff,max} = 45°$, the LEV circulation reaches its maximum at $t/T \approx 4.37$ and then drops. Comparing $\alpha_{eff,max} = 27°$ and 45°, both cases exhibit clear LEV formation (figure 11); however, the LEV pinches off from the downstream boundary layer earlier at $\alpha_{eff,max} = 45°$ due to the larger local α_{eff}. Notably, the case with a circulation plateau ($\alpha_{eff,max} = 27°$) achieves the highest propulsive efficiency (figure 6), demonstrating that neither excessively low nor high $\alpha_{eff,max}$ enables optimal LEV regulation. The formation and role of the secondary structure beneath the LEV, a lambda-shaped vortical structure comprising a positive vortex and a positive wall shear layer, also vary significantly with $\alpha_{eff,max}$. At $\alpha_{eff,max} = 9°$, no secondary structure develops. For $\alpha_{eff,max} = 27°$, the secondary structure initiates almost simultaneously with the onset of the LEV circulation plateau, suggesting that it regulates LEV growth (Akkala & Buchholz 2017). This regulatory mechanism enables sustained thrust production without premature vortex shedding. At $\alpha_{eff,max} = 45°$, the secondary structure exhibits substantially stronger circulation and a more pronounced λ-shaped morphology (figure 11). However, the larger spanwise α_{eff} distribution prevents effective regulation of LEV growth, causing premature circulation decay and consequently reduced propulsive efficiency.

The temporal evolution of circulation and vorticity contours at the inner wing region ($z/b = 0.3$) are presented in figures 12 and 13, respectively. While the overall trends are similar to those at mid-span, several important differences emerge due to the spanwise variation in effective angle of attack.The magnitudes of both LEV and secondary structure circulation are substantially smaller at $z/b = 0.3$ than those at mid-span location, reflecting the reduced local α_{eff} at the inner wing. Correspondingly, LEV pinch-off from the downstream boundary layer occurs only at $\alpha_{eff,max} = 45°$ (figure 13), in contrast to mid-span where pinch-off is observed at both $\alpha_{eff,max} = 27°$ and 45°. Notably, secondary structure formation is contingent upon LEV pinch-off; when the LEV remains attached to its downstream boundary layer, no secondary structure develops. Moreover, the circulation plateau characteristic of mid-span at $\alpha_{eff,max} = 27°$ is absent at all $\alpha_{eff,max}$ values in the

https://doi.org/10.1017/jfm.2026.11974 Published online by Cambridge University Press

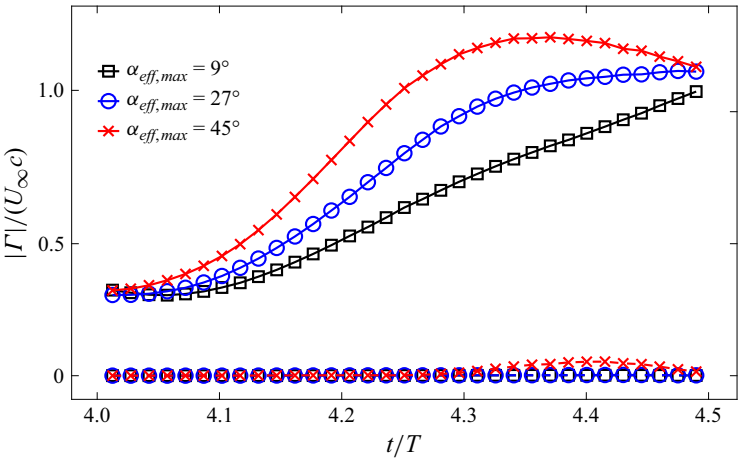


Figure 12. Temporal evolution of the circulations of the LEV and the secondary structure at $z/b = 0.3$. The solid lines represent the LEV (negative vorticity) and the dashed lines represent the secondary structure (positive vorticity).

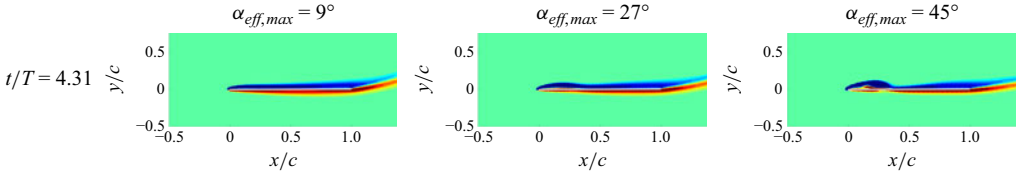


Figure 13. Vorticity contour of the LEV cross-section at $z/b = 0.3$. The legend of the vorticity contour is identical to that of figure 11.

inner wing region as the LEV circulation at $\alpha_{eff,max} = 9°$ and 27° does not reaches its maximum value by the end of the flapping-down period.

These spanwise variations in vortex dynamics reflect the distinct aerodynamic roles of the inner and outer wing regions, as hypothesised by previous studies (Videler *et al.* 2004; Thielicke & Stamhuis 2015). At the inner wing, the relatively small twisting angle (large local α_{eff}) orients force production predominantly in the vertical direction, enabling this region to generate lift. Conversely, at the outer wing, the larger twisting angle (smaller local α_{eff}) redirects force production towards the streamwise direction, making this region the primary source of thrust during cruise flight. This functional differentiation along the span is facilitated by the spanwise distribution of α_{eff} imposed by wing twist.

3.3. *Effects of Φ*

The influence of phase difference Φ between flapping and twisting motions on cycle-averaged aerodynamic performance is presented in figure 14, with the magnitude and direction of the resultant force shown in figure 15. By convention, positive Φ indicates that the wing reaches the prescribed $\alpha_{eff,max}$ earlier during the downstroke. The resultant force magnitude decreases approximately linearly with increasing Φ (figure 14*c*), while its direction remains bounded between 30° and 60° (figure 15). The power consumption coefficient (figure 14*d*) also decreases approximately linearly with increasing Φ. The side force coefficient decreases with increasing Φ (figure 14*b*), but with a smaller decrease rate compared with the resultant force magnitude and the power consumption coefficient. It

https://doi.org/10.1017/jfm.2026.11974 Published online by Cambridge University Press

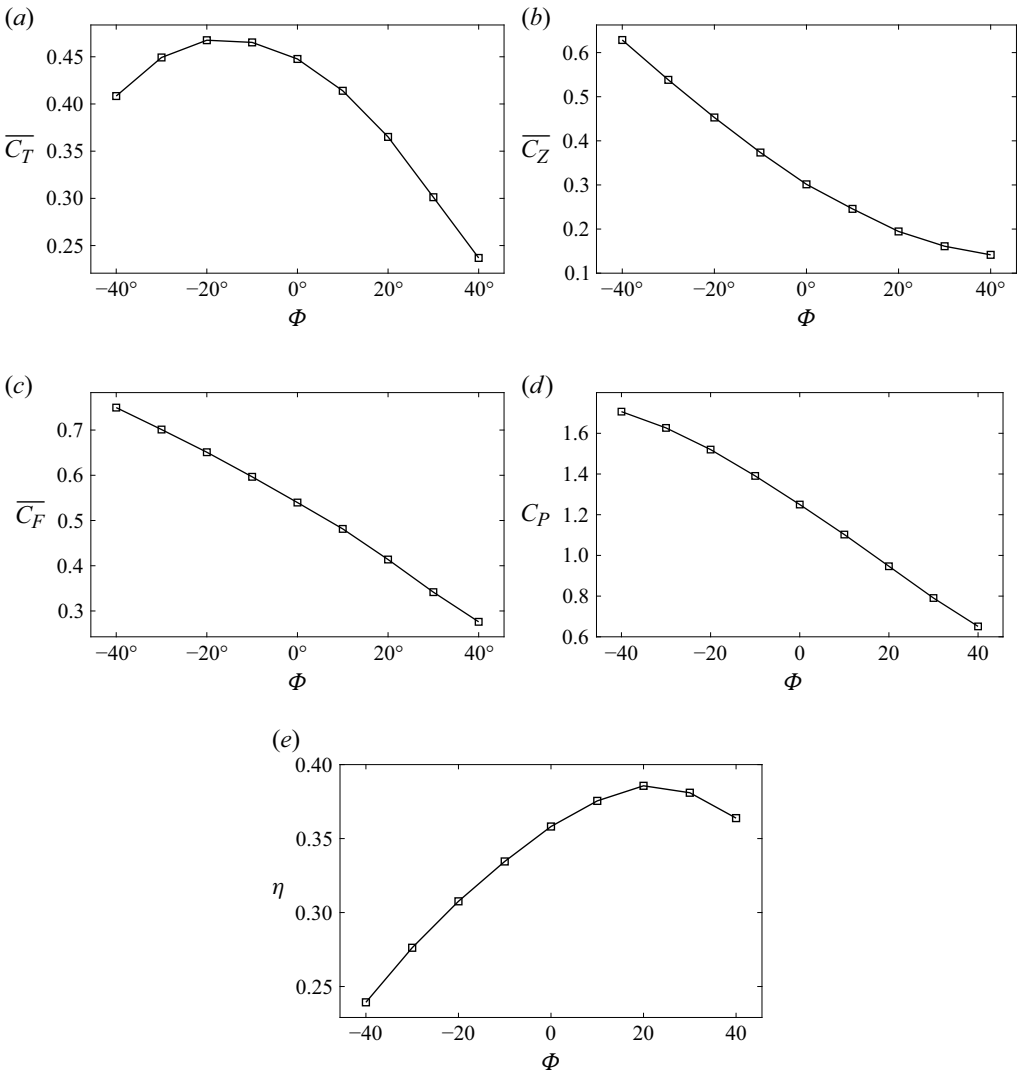


Figure 14. Effects of Φ on (*a*) the average thrust coefficient, (*b*) the average side force coefficient, (*c*) the average resultant force magnitude coefficient, (*d*) the average power consumption coefficient and (*e*) the propulsive efficiency at $St_A = 0.6$, $\alpha_{eff,max} = 27°$ and $Re_c = 1500$.

can be seen that all the force coefficients decrease when the twisting motion is delayed (positive Φ). Notably, thrust production and propulsive efficiency respond differently to phase variation. Maximum thrust is achieved at $\Phi = -20°$ (figure 14*a*), whereas maximum propulsive efficiency occurs at $\Phi = 20°$ (figure 14*e*). This indicates a fundamental trade-off: advancing the twisting motion (negative Φ) enhances thrust generation, while delaying it (positive Φ) improves propulsive efficiency. Despite differences in flapping kinematics and free-stream flow conditions, the present observation is consistent with a previous study on a hovering wing undergoing wing flip (pitching about the mid-chord), wherein an advanced flip was found to enhance lift production (Chen & Wu 2024).

Three-dimensional vortical structures at $\Phi = -20°$, 20° and 40° during the downstroke are presented in figure 16, revealing how phase difference modulates vortex evolution

https://doi.org/10.1017/jfm.2026.11974 Published online by Cambridge University Press

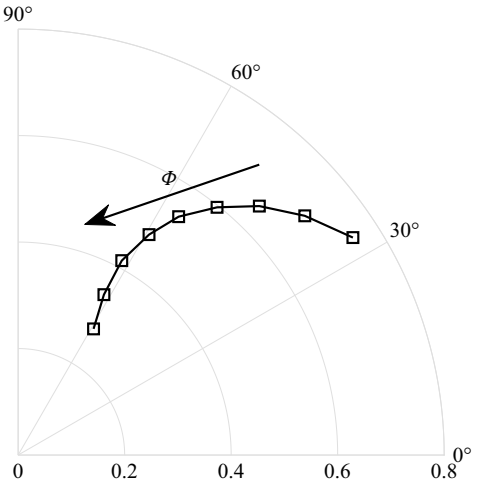


Figure 15. Magnitude (radius) and direction (azimuth angle) of the average resultant force coefficient with increasing Φ. The X direction is along the 90° direction and the Z direction is along the 0° direction. The increase direction of Φ is indicated by the arrow.

and attachment. At the beginning of the downstroke ($t/T = 4.125$), the LEV at $\Phi = 40°$ is slightly larger than the others due to the higher α_{eff} during early downstroke. However, its core pressure is elevated compared with the other cases, indicating weaker suction consistent with figure 14(*c*). Overall, LEV morphology remains similar across all three cases at this early stage. By mid-downstroke ($t/T = 4.250$), significant differences emerge. The LEV exhibits greater strength and lower core pressure when the wing reaches maximum α_{eff} after mid-downstroke ($\Phi = -20°$) compared with when it peaks earlier ($\Phi = 20°$). At $\Phi = 40°$, the LEV begins to shed from the wing and loses coherence. These observations underscore the importance of proper flapping-twisting coordination for generating and maintaining a strong, attached LEV during cruise. During the latter half of the downstroke ($t/T = 4.375$ and 4.500), phase effects become even more pronounced. At $\Phi = -20°$, both LEV and TV maintain coherent structures and remain attached to the wing, sustained by the relatively high spanwise α_{eff} distribution. In contrast, at $\Phi = 20°$ and 40°, the LEV and TV lose coherence and shed into the wake. The underlying mechanism relates to vorticity supply and LEV–wing interaction. Delayed twisting (positive Φ) reduces the influx of leading-edge shear layer vorticity during the second half of the downstroke, starving the LEV and TV while intensifying LEV–wing interaction. Conversely, advanced twisting (negative Φ) sustains vorticity supply to the LEV as the wing decelerates, resulting in a stronger vortex. Furthermore, early twisting reduces LEV–wing interaction, promoting prolonged LEV attachment and explaining the enhanced thrust production observed at negative Φ.

Proper coordination between flapping and twisting motions critically influences both thrust production and propulsive efficiency. The trade-off between these two performance metrics stems from the timing of vortex detachment relative to stroke reversal. Advanced twisting (negative Φ), where the wing reaches maximum α_{eff} later in the downstroke, generates greater thrust, but at the cost of increased drag. This drag penalty arises when vortical structures generated during the previous half-stroke remain attached to the wing at the onset of the subsequent half-stroke. Since the LEV and TV are positioned aft of the wing's centroid, their persistence during stroke reversal produces a drag force that opposes the wing's motion. In contrast, delayed twisting (positive Φ) promotes earlier vortex

https://doi.org/10.1017/jfm.2026.11974 Published online by Cambridge University Press

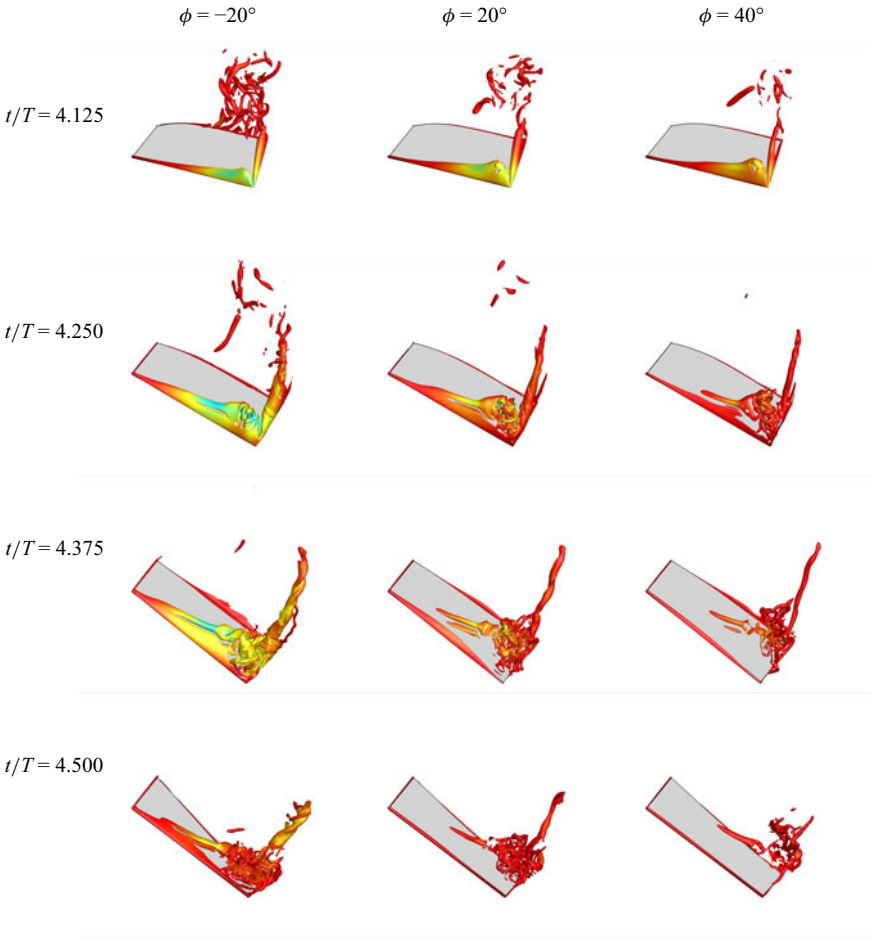


Figure 16. The 3-D vortical structures identified by $Q = 50$ coloured by the pressure coefficient at $St_A = 0.6$ and $\alpha_{eff,max} = 27°$ for $\Phi = -20°$, 20° and 40° in the fifth flapping cycle. The legend of the pressure coefficient is identical to that of figure 8.

detachment and thereby enhances propulsive efficiency. By reducing leading-edge and tip shear layer influx during the latter half of each half-stroke, delayed twisting facilitates LEV and TV shedding before stroke reversal. This timing ensures that the wing begins each half-stroke with minimal residual vortical structures, thereby reducing form drag and improving efficiency. Thus, while advanced twisting maximises instantaneous force production, delayed twisting optimises the power economy by minimising parasitic drag associated with vortex–wing interaction across stroke cycles.

The temporal evolution of the LEV and secondary structure circulations at $z/b = 0.3$ and 0.6 during the downstroke is presented in figure 17, with vorticity contours at $z/b = 0.6$ and $t/T = 4.45$ shown in figure 18. Peak LEV circulation magnitude decreases monotonically with increasing Φ at both spanwise locations. Early in the downstroke, cases with larger Φ exhibit slightly higher negative vorticity circulation due to the elevated α_{eff} during this phase. Comparing $\Phi = -20°$ and 20° – which share the same maximum twisting angle but differ in timing – reveals that the former achieves substantially higher peak LEV circulation. This demonstrates that early twisting during the downstroke enhances LEV growth. At the inner wing ($z/b = 0.3$), no positive vorticity

https://doi.org/10.1017/jfm.2026.11974 Published online by Cambridge University Press

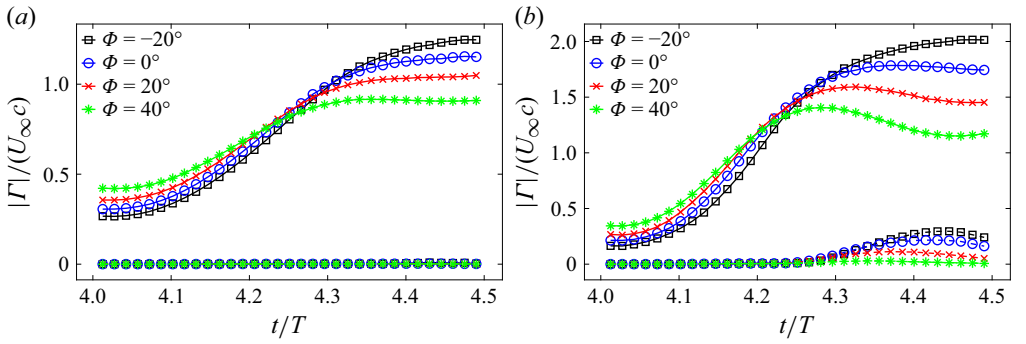


Figure 17. Temporal evolution of the circulations of the LEV and the secondary structure. The solid lines represent the LEV (negative vorticity) and the dashed lines represent the secondary structure (positive vorticity). (*a*) $z/b = 0.3$ and (*b*) $z/b = 0.6$.

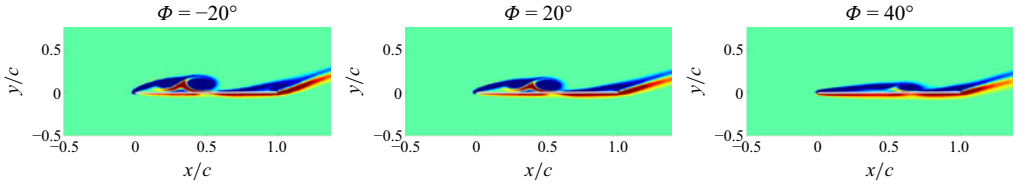


Figure 18. Vorticity contour of the LEV cross-section at $z/b = 0.6$ for $\Phi = -20°$, 0° and 40° at $t/T = 4.45$. The legend of the vorticity contour is identical to that of figure 11.

accumulates beneath the LEV for any Φ value, indicating that the LEV remains attached to its downstream boundary layer and no secondary structure formation. Complete LEV detachment typically triggers formation of a half-saddle point, which promotes secondary structure development through vorticity accumulation (Rival *et al.* 2014); the absence of this accumulation confirms incomplete separation at this inboard location. At $z/b = 0.6$, positive vorticity accumulation occurs for all cases, indicating LEV detachment and secondary structure formation. LEV circulation evolution remains similar across all Φ values until mid-downstroke (figure 17*b*); substantial differences emerge only after secondary structure initiation. Secondary structure circulation strength decreases with increasing Φ, corresponding to variations in shear layer orientation. As shown in figure 18, the angle between the leading-edge shear layer and the wing surface decreases with increasing Φ, consistent with the reduced α_{eff} during late downstroke. At higher α_{eff} (negative Φ), the steeper shear layer angle sustains continued LEV growth. Conversely, increasing Φ causes the LEV to migrate closer to the trailing edge by the end of the downstroke, facilitating faster vortex shedding at the onset of the upstroke and thereby reducing drag. Thus, Φ primarily modulates propulsive performance by controlling shear layer orientation and, consequently, LEV growth dynamics.

4. Conclusions

Numerical simulations have been performed to investigate the effects of spanwise twisting on the aerodynamic force production and the LEV dynamics of a low aspect-ratio (AR) flapping wing. Several key findings emerge from this study. For each Strouhal number St_A, an optimal effective angle of attack $\alpha_{eff,max}$ exists that balances thrust production

https://doi.org/10.1017/jfm.2026.11974 Published online by Cambridge University Press

and propulsive efficiency for a low AR flapping wing, consistent with previous two-dimensional flapping foil studies (Schouveiler *et al.* 2005). Importantly, the resultant force magnitude remains relatively insensitive to $\alpha_{eff,max}$ variations at fixed St_A. Rather than modulating overall force production, spanwise twisting primarily reallocates force production between the streamwise and spanwise directions. This force reallocation mechanism enables maximum propulsive efficiency ($\eta = 0.36$) at $St_A = 0.6$ and $\alpha_{eff,max} = 27°$. At this optimal condition, the LEV detaches from its downstream boundary layer, triggering the secondary structure, a positive vortical structure, formation beneath the LEV. Circulation analysis reveals that the secondary structure regulates LEV growth, establishing a circulation plateau during the latter half of the downstroke ($t/T = 4.3$–4.5). This regulated vortex growth is critical to achieving high propulsive efficiency. In contrast, at the inner wing ($z/b = 0.3$), the LEV remains attached to the downstream boundary layer for $\alpha_{eff,max} = 9°$ and $27°$ due to the smaller local α_{eff}. This spanwise variation in vortex dynamics reflects functional differentiation along the wing: the inboard region maintains attached flow and generates lift through steady aerodynamic mechanisms, while the outboard region exploits unsteady LEV dynamics to produce thrust. Phase difference Φ between twisting and flapping motions significantly affects the thrust-efficiency trade-off. Delayed twisting (positive Φ), where maximum α_{eff} is reached after mid-downstroke, enhances propulsive efficiency by promoting vortex shedding before stroke reversal and thereby reducing form drag. Conversely, advanced twisting (negative Φ), where maximum twisting occurs early in the downstroke, sustains higher α_{eff} during the power phase and thus amplifies thrust production. This finding highlights the importance of precise kinematic coordination in optimising the low *AR* flapping wing performance for different flight objectives.

Funding. This work was conducted with the assistance of computational resources from the National Computational Infrastructure (NCI), supported by the Australian Government.

Declaration of interests. The authors report no conflict of interest.

Appendix A. Verification of result reliability

A.1. *Grids dependency study*

To study the effects of the grid resolution on the results, simulations of three mesh resolutions are conducted at $Re = 4500$ for $St_A = 0.6$, $\alpha_0 = 36°$ and $\Phi = 0$. Here, $\Delta x = c/64$ is the grid resolution in the finest block for the coarse mesh set-up, $\Delta x = c/128$ is the grid size in the finest block for the medium mesh set-up and $\Delta x = c/256$ is the grid size in the finest block for the fine mesh set-up. The time histories of the drag, lift and side force coefficients are shown in figure 19. With increasing the mesh resolution, the difference in C_D decreases, where the viscous friction on the wing is resolved well by using medium and fine grids. Here, C_L and C_Z are dominated by the pressure-induced force, which is less sensitive to the grid resolution. It can be seen that the simulation results at $Re = 4500$ are accurate enough using the medium mesh set-up. Therefore, simulation results at $Re = 1500$ using the medium mesh set-up are converged.

A.2. *Wing area change in twisting*

The wing area change for $St_A = 1.0$ and $\alpha_{eff} = 9°$ (case with the largest twisting) in one flapping cycle is shown in figure 20. It is found that the wing area at the maximum twisting time instance ($t/T = 0.25$ and 0.75) is approximately 3.5 % larger than the non-twisting time instance ($t/T = 0$ and 1). The area change is very small compared with the change

https://doi.org/10.1017/jfm.2026.11974 Published online by Cambridge University Press

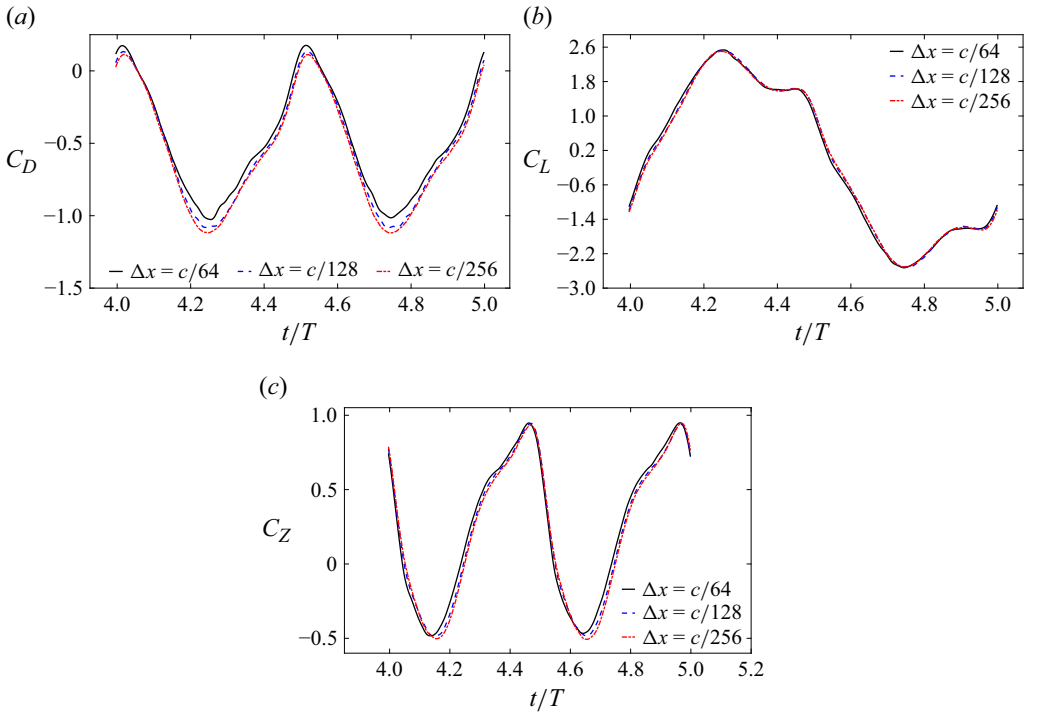


Figure 19. Effects of grid resolution on (*a*) the drag coefficient, (*b*) the lift coefficient and (*c*) the side force coefficient at $Re = 4500$.

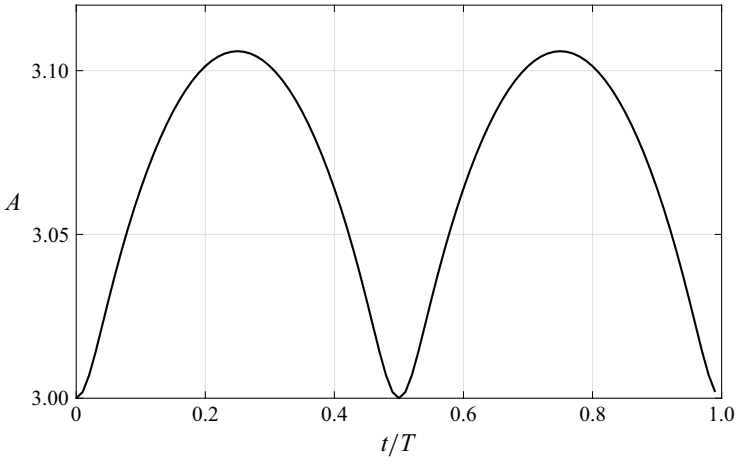


Figure 20. Wing area in one flapping cycle for $St_A = 1.0$ and $\alpha_{eff} = 9°$. This is the case with the largest wing area change as the maximum twisting effects.

in the aerodynamic force coefficients with increasing $\alpha_{eff,max}$ (decreasing twisting), as shown in figure 4. Thus, it can be considered that the effects of wing area change on the aerodynamics of the wing are negligible.

https://doi.org/10.1017/jfm.2026.11974 Published online by Cambridge University Press

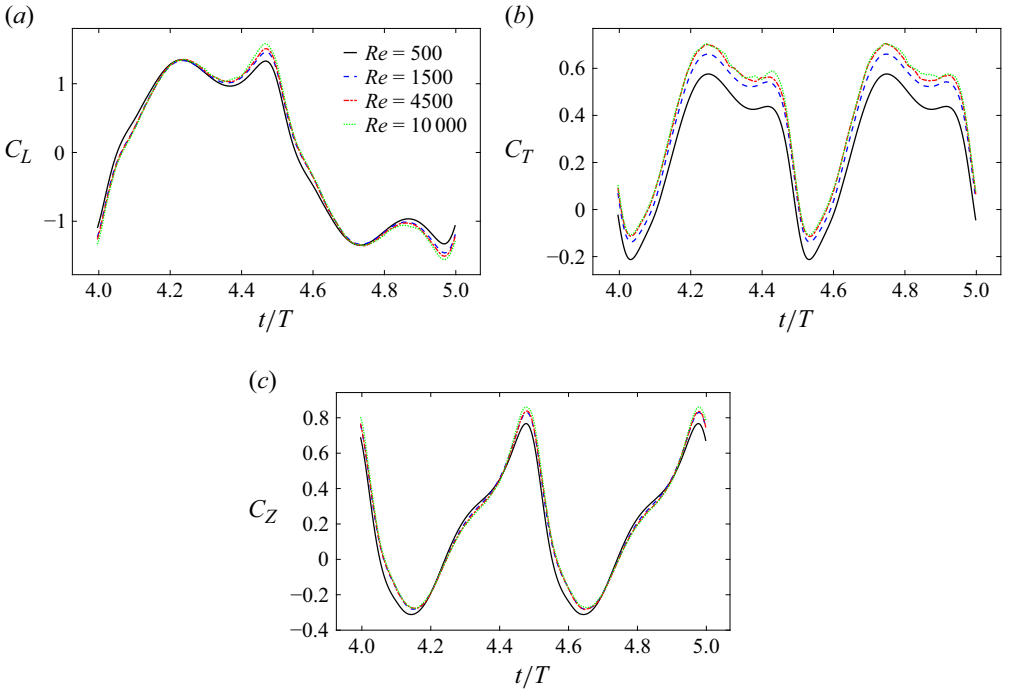


Figure 21. Time histories of (*a*) the lift coefficient, (*b*) the thrust coefficient and (*c*) the side force coefficient for $St_A = 0.6$, $\alpha_{eff,max} = 27°$ and $\Phi = 20°$ at $Re = 500$, 1500, 4500 and 10 000 during the fourth flapping cycle.

A.3. *Effects of Reynolds numbers*

The time histories of the lift (panel *a*), thrust (panel *b*) and side force coefficient (panel *c*) for the cases of $St_A = 0.6$ and $\alpha_{eff,max} = 27°$ at $Re = 500$, 1500, 4500 and 10 000 are shown in figure 21. The difference in C_L and C_Z between the three Reynolds numbers is slight because the wing inertial force due to acceleration and pressure-induced force from the vortices, an inviscid process, dominates force production in the non-streamwise direction. For C_T, the variation is similar among the three Reynolds numbers, but the magnitude of C_T is higher at $Re = 1500$, 4500 and 10 000 due to the smaller skin friction, where the increase in the magnitude of C_T decreases with increasing Re being consistent with the laminar force scaling of flapping wings found in previous studies (Senturk & Smits 2019; Verma *et al.* 2022). Because of the limited differences in the aerodynamic performance within the range of Re $O(10^3)$ to $O(10^5)$ for flapping wings (Anderson *et al.* 1998; Zhang *et al.* 2022*a*), only the results at $Re = 1500$ are discussed and analysed in this work.

References

Addo-Akoto, R., Han, J.-S. & Han, J.-H. 2021 Roles of wing flexibility and kinematics in flapping wing aerodynamics. *J. Fluids Struct.* **104**, 103317.

Aidun, C.K. & Clausen, J.R. 2010 Lattice-Boltzmann method for complex flows. *Annu. Rev. Fluid Mech.* **42** (1), 439–472.

Akkala, J.M. & Buchholz, J.H.J. 2017 Vorticity transport mechanisms governing the development of leading-edge vortices. *J. Fluid Mech.* **829**, 512–537.

Alexander, D.E. 2002 *Nature's Flyers: Birds, Insects, and the Biomechanics of Flight*. JHU Press.

Anderson, J.M., Streitlien, K., Barrett, D.S. & Triantafyllou, M.S. 1998 Oscillating foils of high propulsive efficiency. *J. Fluid Mech.* **360**, 41–72.

Azuma, A. 2012 *The Biokinetics of Flying and Swimming*. Springer Science & Business Media.

https://doi.org/10.1017/jfm.2026.11974 Published online by Cambridge University Press

BAIK, Y.S., BERNAL, L.P., GRANLUND, K. & OL, M.V. 2012 Unsteady force generation and vortex dynamics of pitching and plunging aerofoils. *J. Fluid Mech.* **709**, 37–68.
BOMPHREY, R.J., NAKATA, T., PHILLIPS, N. & WALKER, S.M. 2017 Smart wing rotation and trailing-edge vortices enable high frequency mosquito flight. *Nature* **544** (7648), 92–95.
BOZKURTTAS, M., MITTAL, R., DONG, H., LAUDER, G.V. & MADDEN, P. 2009 Low-dimensional models and performance scaling of a highly deformable fish pectoral fin. *J. Fluid Mech.* **631**, 311–342.
CARR, L.W. 1988 Progress in analysis and prediction of dynamic stall. *J. Aircraft* **25** (1), 6–17.
CARRUTHERS, A.C., THOMAS, A.L.R. & TAYLOR, G.K. 2007 Automatic aeroelastic devices in the wings of a steppe eagle *Aquila nipalensis*. *J. Expl Biol.* **210** (23), 4136–4149.
CHEN, L. & WU, J. 2024 Coexistence of dual wing–wake interaction mechanisms during the rapid rotation of flapping wings. *J. Fluid Mech.* **987**, A16.
CHEN, S. & DOOLEN, G.D. 1998 Lattice Boltzmann method for fluid flows. *Annu. Rev. Fluid Mech.* **30** (1), 329–364.
CHIN, D.D. & LENTINK, D. 2016 Flapping wing aerodynamics: from insects to vertebrates. *J. Expl Biol.* **219** (7), 920–932.
CHOUDHRY, A., LEKNYS, R., ARJOMANDI, M. & KELSO, R. 2014 An insight into the dynamic stall lift characteristics. *Exp. Therm. Fluid Sci.* **58**, 188–208.
COREIXAS, C., WISSOCQ, G., PUIGT, G., BOUSSUGE, J.-F. & SAGAUT, P. 2017 Recursive regularization step for high-order lattice Boltzmann methods. *Phys. Rev. E* **96**, 033306.
DICKINSON, M.H., LEHMANN, F.-O. & SANE, S.P. 1999 Wing rotation and the aerodynamic basis of insect flight. *Science* **284** (5422), 1954–1960.
DU, G. & SUN, M. 2010 Effects of wing deformation on aerodynamic forces in hovering hoverflies. *J. Expl Biol.* **213** (13), 2273–2283.
ELDREDGE, J.D. & JONES, A.R. 2019 Leading-edge vortices: mechanics and modeling. *Annu. Rev. Fluid Mech.* **51** (1), 75–104.
ELLINGTON, C.P. 1999 The novel aerodynamics of insect flight: applications to micro-air vehicles. *J. Expl Biol.* **202** (23), 3439–3448.
ELLINGTON, C.P., VAN DEN BERG, C., WILLMOTT, A.P. & THOMAS, A.L.R. 1996 Leading-edge vortices in insect flight. *Nature* **384** (6610), 626–630.
FORD, C.W.P. & BABINSKY, H. 2013 Lift and the leading-edge vortex. *J. Fluid Mech.* **720**, 280–313.
FU, J.-J., HEFLER, C., QIU, H.-H. & SHYY, W. 2014 Effects of aspect ratio on flapping wing aerodynamics in animal flight. *Acta Mechanica Sin.* **30** (6), 776–786.
GARMANN, D.J. & VISBAL, M.R. 2014 Dynamics of revolving wings for various aspect ratios. *J. Fluid Mech.* **748**, 932–956.
GOLDSTEIN, D., HANDLER, R. & SIROVICH, L. 1993 Modeling a no-slip flow boundary with an external force field. *J. Comput. Phys.* **105** (2), 354–366.
GRIFFITH, B.E. & PATANKAR, N.A. 2020 Immersed methods for fluid–structure interaction. *Annu. Rev. Fluid Mech.* **52** (1), 421–448.
GUO, Z., ZHENG, C. & SHI, B. 2002 Discrete lattice effects on the forcing term in the lattice Boltzmann method. *Phys. Rev. E* **65**, 046308.
HAN, J.-S., CHANG, J.W. & CHO, H.-K. 2015 Vortices behavior depending on the aspect ratio of an insect-like flapping wing in hover. *Exp. Fluids* **56** (9), 181.
HARBIG, R.R., SHERIDAN, J. & THOMPSON, M.C. 2013 Reynolds number and aspect ratio effects on the leading-edge vortex for rotating insect wing planforms. *J. Fluid Mech.* **717**, 166–192.
HEDRICK, T.L., CHENG, B. & DENG, X. 2009 Wingbeat time and the scaling of passive rotational damping in flapping flight. *Science* **324** (5924), 252–255.
HOVER, F.S., HAUGSDAL, Ø. & TRIANTAFYLLOU, M.S. 2004 Effect of angle of attack profiles in flapping foil propulsion. *J. Fluids Struct.* **19** (1), 37–47.
HUANG, Q., BHAT, S.S., YEO, E.C., YOUNG, J., LAI, J.C.S., TIAN, F.-B. & RAVI, S. 2023 Power synchronisations determine the hovering flight efficiency of passively pitching flapping wings. *J. Fluid Mech.* **974**, A41.
HUANG, Q., LIU, Z., WANG, L., RAVI, S., YOUNG, J., LAI, J.C.S. & TIAN, F.-B. 2022 Streamline penetration, velocity error, and consequences of the feedback immersed boundary method. *Phys. Fluids* **34** (9), 097101.
HUANG, W.-X. & TIAN, F.-B. 2019 Recent trends and progress in the immersed boundary method. *Proc. Inst. Mech. Engrs C: J. Mech. Engng Sci.* **233** (23–24), 7617–7636.
HUBEL, T. 2007 Untersuchungen zur instationären aerodynamik an einem vogelähnlichen flügelschlagmodell. PhD thesis, Technische Universität, Darmstadt.
JEONG, J. & HUSSAIN, F. 1995 On the identification of a vortex. *J. Fluid Mech.* **285**, 69–94.

https://doi.org/10.1017/jfm.2026.11974 Published online by Cambridge University Press

JIN, B.R., JI, X., RAVI, S., YOUNG, J., PEREIRA, G.G. & TIAN, F.-B. 2025 Lift increment scaling and its failure due to the leading-edge vortex detachment transition for a flapping wing under perturbations. *J. Fluid Mech.* **1022**, A28.

JIN, B.R., WANG, L., RAVI, S., YOUNG, J., LAI, J.C.S. & TIAN, F.-B. 2024 Enhancing tip vortices to improve the lift production through shear layers in flapping-wing flow control. *J. Fluid Mech.* **999**, A25.

KRÜGER, T., KUSUMAATMAJA, H., KUZMIN, A., SHARDT, O., SILVA, G. & VIGGEN, E.M. 2017 *The Lattice Boltzmann Method*. Springer Cham.

LATT, J. & CHOPARD, B. 2006 Lattice Boltzmann method with regularized pre-collision distribution functions. *Maths Comput. Simul.* **72** (2), 165–168.

LEE, J., CHOI, H. & KIM, H.-Y. 2015 A scaling law for the lift of hovering insects. *J. Fluid Mech.* **782**, 479–490.

LIU, H., WANG, S. & LIU, T. 2024 Vortices and forces in biological flight: insects, birds, and bats. *Annu. Rev. Fluid Mech.* **56** (1), 147–170.

MACKENZIE, D. 2012 A flapping of wings. *Science* **335** (6075), 1430–1433.

MAXWORTHY, T. 1979 Experiments on the Weis–Fogh mechanism of lift generation by insects in hovering flight. Part 1. Dynamics of the 'fling'. *J. Fluid Mech.* **93** (1), 47–63.

MAXWORTHY, T. 1981 The fluid dynamics of insect flight. *Annu. Rev. Fluid Mech.* **13** (1), 329–350.

MCCROSKEY, W.J. 1982 Unsteady airfoils. *Annu. Rev. Fluid Mech.* **14**, 285–311.

MCGAHAN, J. 1973 Flapping flight of the Andean condor in nature. *J. Expl Biol.* **58** (1), 239–253.

MEDINA, A. & JONES, A.R. 2016 Leading-edge vortex burst on a low-aspect-ratio rotating flat plate. *Phys. Rev. Fluids* **1**, 044501.

MITTAL, R. & IACCARINO, G. 2005 Immersed boundary methods. *Annu. Rev. Fluid Mech.* **37** (1), 239–261.

MOUNTCASTLE, A.M. & COMBES, S.A. 2013 Wing flexibility enhances load-lifting capacity in bumblebees. *Proc. R. Soc. Lond. B: Biol. Sci.* **280** (1759), 20130531.

MUIJRES, F.T., JOHANSSON, L.C., BARFIELD, R., WOLF, M., SPEDDING, G.R. & HEDENSTRÖM, A. 2008 Leading-edge vortex improves lift in slow-flying bats. *Science* **319** (5867), 1250–1253.

MULLENERS, K. & RAFFEL, M. 2012 The onset of dynamic stall revisited. *Exp. Fluids* **52**, 779–793.

NAKATA, T. & LIU, H. 2012 A fluid–structure interaction model of insect flight with flexible wings. *J. Comput. Phys.* **231** (4), 1822–1847.

NGUYEN, K., AU, L.T.K., PHAN, H.-V., PARK, S.H. & PARK, H.C. 2021 Effects of wing kinematics, corrugation, and clap-and-fling on aerodynamic efficiency of a hovering insect-inspired flapping-wing micro air vehicle. *Aerosp. Sci. Technol.* **118**, 106990.

NORBERG, U.M. 1990 *Vertebrate Flight*. Springer.

PENNYCUICK, C.J. 1989 Span-ratio analysis used to estimate effective lift: drag ratio in the double-crested cormorant Phalacrocorax auritus from field observations. *J. Expl Biol.* **142** (1), 1–15,

PESAVENTO, U. & WANG, Z.J. 2009 Flapping wing flight can save aerodynamic power compared to steady flight. *Phys. Rev. Lett.* **103**, 118102.

PESKIN, C.S. 2002 The immersed boundary method. *Acta Numerica* **11**, 479–517.

PHAN, H.V. & PARK, H.C. 2020 Mechanisms of collision recovery in flying beetles and flapping-wing robots. *Science* **370** (6521), 1214–1219.

PHILLIPS, N., KNOWLES, K. & BOMPHREY, R.J. 2015 The effect of aspect ratio on the leading-edge vortex over an insect-like flapping wing. *Bioinspir. Biomim.* **10** (5), 056020.

PLATZER, M.F., JONES, K.D., YOUNG, J. & LAI, J.C.S. 2008 Flapping wing aerodynamics: progress and challenges. *AIAA J.* **46** (9), 2136–2149.

PULLIN, D.I. & WANG, Z.J. 2004 Unsteady forces on an accelerating plate and application to hovering insect flight. *J. Fluid Mech.* **509**, 1–21.

RAFEE NEKOO, S., RASHAD, R., DE WAGTER, C., FULLER, S.B., CROON, G., STRAMIGIOLI, S. & OLLERO, A. 2025 A review on flapping-wing robots: recent progress and challenges. *Intl J. Robot. Res.* **44** (14), 2305–2339.

RIVAL, D.E., KRIEGSEIS, J., SCHAUB, P., WIDMANN, A. & TROPEA, C. 2014 Characteristic length scales for vortex detachment on plunging profiles with varying leading-edge geometry. *Exp. Fluids* **55** (1), 1–8.

ROSÉN, M., SPEDDING, G.R. & HEDENSTROÖM, A. 2004 The relationship between wingbeat kinematics and vortex wake of a thrush nightingale. *J. Expl Biol.* **207** (24), 4255–4268.

SANE, S.P. 2003 The aerodynamics of insect flight. *J. Expl Biol.* **206** (23), 4191–4208.

SCHOUVEILER, L., HOVER, F.S. & TRIANTAFYLLOU, M.S. 2005 Performance of flapping foil propulsion. *J. Fluids Struct.* **20** (7), 949–959.

SENTURK, U. & SMITS, A.J. 2019 Reynolds number scaling of the propulsive performance of a pitching airfoil. *AIAA J.* **57** (7), 2663–2669.

https://doi.org/10.1017/jfm.2026.11974 Published online by Cambridge University Press

SHAHZAD, A., TIAN, F.-B., YOUNG, J. & LAI, J.C.S. 2018 Effects of hawkmoth-like flexibility on the aerodynamic performance of flapping wings with different shapes and aspect ratios. *Phys. Fluids* **30** (9), 091902.

SHOELE, K. & ZHU, Q. 2013 Performance of a wing with nonuniform flexibility in hovering flight. *Phys. Fluids* **25** (4), 041901.

SHYY, W., AONO, H., CHIMAKURTHI, S.K., TRIZILA, P., KANG, C.-K., CESNIK, C.E.S. & LIU, H. 2010 Recent progress in flapping wing aerodynamics and aeroelasticity. *Prog. Aerosp. Sci.* **46** (7), 284–327.

SHYY, W., LIAN, Y., TANG, J., VIIERU, D. & LIU, H. 2008 *Aerodynamics of Low Reynolds Number Flyers*. Cambridge University Press.

SHYY, W. & LIU, H. 2007 Flapping wings and aerodynamic lift: the role of leading-edge vortices. *AIAA J.* **45** (12), 2817–2819.

TAYLOR, G.K., NUDDS, R.L. & THOMAS, A.L.R. 2003 Flying and swimming animals cruise at a Strouhal number tuned for high power efficiency. *Nature* **425** (6959), 707–711.

THIELICKE, W. & STAMHUIS, E.J. 2015 The influence of wing morphology on the three-dimensional flow patterns of a flapping wing at bird scale. *J. Fluid Mech.* **768**, 240–260.

THIELICKE, W. & STAMHUIS, E.J. 2018 The effects of wing twist in slow-speed flapping flight of birds: trading brute force against efficiency. *Bioinspir. Biomim.* **13** (5), 056015.

THOMAS, A.L.R. & HEDENSTRÖM, A. 1998 The optimum flight speeds of flying animals. *J. Avian Biol.* **29** (4), 469–477.

TOBALSKE, B.W. & DIAL, K.P. 1996 Flight kinematics of black-billed magpies and pigeons over a wide range of speeds. *J. Expl Biol.* **199** (2), 263–280.

USHERWOOD, J.R. & ELLINGTON, C.P. 2002 The aerodynamics of revolving wings I. Model hawkmoth wings. *J. Expl Biol.* **205** (11), 1547–1564.

VERMA, S., FREEMAN, B.R.S. & HEMMATI, A. 2022 Effects of Reynolds number and average angle of attack on the laminar scaling of oscillating foils. *Phys. Fluids* **34** (3), 031905.

VIDELER, J.J., STAMHUIS, E.J. & POVEL, G.D.E. 2004 Leading-edge vortex lifts swifts. *Science* **306** (5703), 1960–1962.

VREMAN, A.W. 2004 An eddy-viscosity subgrid-scale model for turbulent shear flow: algebraic theory and applications. *Phys. Fluids* **16** (10), 3670–3681.

WALKER, S.M., THOMAS, A.L.R. & TAYLOR, G.K. 2009 Photogrammetric reconstruction of high-resolution surface topographies and deformable wing kinematics of tethered locusts and free-flying hoverflies. *J. R. Soc. Interface* **6** (33), 351–366.

WALKER, S.M., THOMAS, A.L.R. & TAYLOR, G.K. 2012 Operation of the alula as an indicator of gear change in hoverflies. *J. R. Soc. Interface* **9** (71), 1194–1207.

WANG, L., LIU, Z., JIN, B.R., HUANG, Q., YOUNG, J. & TIAN, F.-B. 2024 Wall-modeled large eddy simulation in the immersed boundary-lattice Boltzmann method. *Phys. Fluids* **36** (3), 035167.

WANG, Z.J. 2005 Dissecting insect flight. *Annu. Rev. Fluid Mech.* **37** (1), 183–210.

WILKINS, P.C. & KNOWLES, K. 2009 The leading-edge vortex and aerodynamics of insect-based flapping-wing micro air vehicles. *Aeronaut. J.* **113** (1142), 253–262.

WOOTTON, R.J. 1992 Functional morphology of insect wings. *Annu. Rev. Entomol.* **37** (1992), 113–140.

WOOTTON, R.J. 1993 Leading edge section and asymmetric twisting in the wings of flying butterflies (Insecta, Papilionoidea). *J. Expl Biol.* **180** (1), 105–117.

WU, J., CHENG, C., ZHANG, Y., TANG, P., ZHOU, C., CAO, H. & CHEN, L. 2026 Design of a hover-capable flapping wing micro air vehicle with abdomen-wing coupled control. *Chin. J. Aeronaut.* **39** (4), 103807.

XU, H. & SAGAUT, P. 2013 Analysis of the absorbing layers for the weakly-compressible lattice Boltzmann methods. *J. Comput. Phys.* **245**, 14–42.

YOUNG, J., LAI, J.C.S. & PLATZER, M.F. 2014 A review of progress and challenges in flapping foil power generation. *Prog. Aerosp. Sci.* **67**, 2–28.

YOUNG, J., WALKER, S.M., BOMPHREY, R.J., TAYLOR, G.K. & THOMAS, A.L.R. 2009 Details of insect wing design and deformation enhance aerodynamic function and flight efficiency. *Science* **325** (5947), 1549–1552.

ZHANG, D., HUANG, Q.-G., PAN, G., YANG, L.-M. & HUANG, W.-X. 2022*a* Vortex dynamics and hydrodynamic performance enhancement mechanism in batoid fish oscillatory swimming. *J. Fluid Mech.* **930**, A28.

ZHANG, D., PAN, G., CHAO, L. & ZHANG, Y. 2018 Effects of Reynolds number and thickness on an undulatory self-propelled foil. *Phys. Fluids* **30** (7), 071902.

ZHANG, J., ZHAO, N. & QU, F. 2022*b* Bio-inspired flapping wing robots with foldable or deformable wings: a review. *Bioinspir. Biomim.* **18** (1), 011002.

https://doi.org/10.1017/jfm.2026.11974 Published online by Cambridge University Press

ZHAO, L., HUANG, Q., DENG, X. & SANE, S.P. 2010 Aerodynamic effects of flexibility in flapping wings. *J. R. Soc. Interface* **7** (44), 485–497.

ZHU, X., HE, G. & ZHANG, X. 2014 Numerical study on hydrodynamic effect of flexibility in a self-propelled plunging foil. *Comput. Fluids* **97**, 1–20.

ZURMAN-NASUTION, A.N., GANAPATHISUBRAMANI, B. & WEYMOUTH, G.D. 2021 Effects of aspect ratio on rolling and twisting foils. *Phys. Rev. Fluids* **6**, 013101.

https://doi.org/10.1017/jfm.2026.11974 Published online by Cambridge University Press